



**HAL**  
open science

# Boron isotope fractionation during the formation of amorphous calcium carbonates and their transformation to Mg-calcite and aragonite

V. Mavromatis, B. Purgstaller, P. Louvat, L. Faure, V. Montouillout, J. Gaillardet, J. Schott

## ► To cite this version:

V. Mavromatis, B. Purgstaller, P. Louvat, L. Faure, V. Montouillout, et al.. Boron isotope fractionation during the formation of amorphous calcium carbonates and their transformation to Mg-calcite and aragonite. *Geochimica et Cosmochimica Acta*, 2021, 315, pp.152-171. 10.1016/j.gca.2021.08.041 . hal-03408229

**HAL Id: hal-03408229**

**<https://hal.science/hal-03408229>**

Submitted on 29 Oct 2021

**HAL** is a multi-disciplinary open access archive for the deposit and dissemination of scientific research documents, whether they are published or not. The documents may come from teaching and research institutions in France or abroad, or from public or private research centers.

L'archive ouverte pluridisciplinaire **HAL**, est destinée au dépôt et à la diffusion de documents scientifiques de niveau recherche, publiés ou non, émanant des établissements d'enseignement et de recherche français ou étrangers, des laboratoires publics ou privés.

# **Boron isotope fractionation during the formation of amorphous calcium carbonates and their transformation to Mg-calcite and aragonite**

Μαυρομάτης Β. (Mavromatis V.)<sup>1,\*</sup>, Purgstaller B.<sup>2</sup>, Louvat P.<sup>3</sup>, Faure L.<sup>3</sup>, Montouillout V.<sup>4</sup>, Gaillardet J.<sup>3</sup>, Schott J.<sup>1</sup>

<sup>1</sup>Geosciences Environnement Toulouse (GET), CNRS, UMR5563, 14 Avenue Edouard Belin, 31400, Toulouse, France

<sup>2</sup>Institute of Applied Geosciences, Graz University of Technology, Rechbauerstrasse 12, 8010, Graz, Austria

<sup>3</sup>Institut de Physique du Globe de Paris, Sorbonne Paris Cité, Univ. Paris Diderot, UMR 7154 CNRS, 75005 Paris, France

<sup>4</sup>CEMHTI CNRS UPR3079, Université d'Orléans, 45071 Orléans cedex 1, France

\*vasileios.mavromatis@get.omp.eu

## **Abstract**

The non-classical crystallization pathway of carbonate minerals proceeds through the initial formation of an amorphous precursor phase and commonly takes place during biomineralization. Although the isotopic composition of marine calcifiers is often used to reconstruct paleo-environmental conditions, the impact of the crystallization pathway followed by these organisms on the isotope composition of their skeletons has rarely been quantified. This study presents the first examination of B partitioning and isotope fractionation during CaCO<sub>3</sub> formation via an amorphous calcium carbonate phase, which provides new insights into the incorporation of B into marine calcite and aragonite that form via this route. Boron concentrations and isotope compositions of the fluids and the formed solids were characterized during the course of experiments that lasted two years and were performed at 25°C under controlled pH conditions. The results suggest that during Mg-ACC formation, B distribution coefficients are 1.5-4 orders of magnitude higher than those reported earlier in the literature for calcite and aragonite. Additionally, B isotope fractionation during Mg-ACC formation is strongly affected by the continuous exchange of solutes between the nanoporous solid phase and the bulk fluid. The isotope composition of the transient amorphous phase is not inherited in the crystalline carbonate mineral phase that ultimately forms, because crystallization proceeds via a continuous dissolution/re-precipitation process and/or chemical/isotope exchange between the solid surface and the fluid. Interestingly, the isotope fractionation between the fluid and the final crystalline products is different from those achieved in earlier studies where mineral growth proceeded via the standard mechanism of ion-by-ion addition of solutes to advancing steps. The B isotope fractionations measured in this study are in good agreement with results of equilibrium first principle calculations for calcite and aragonite (Balan et al., 2018) except in the case of calcite formed at pH = 8.9, suggesting that changes in aqueous speciation (i.e. increase of NaB(OH)<sub>4</sub><sup>0</sup> and CO<sub>3</sub><sup>2-</sup> concentrations) may be responsible for slight changes of the calcite BO<sub>4</sub> environment and isotope composition. It is expected that

this study will help to better decipher the mechanisms controlling B isotope fractionation during the non-classical growth of calcium carbonates involving the formation of transient amorphous precursors.

**Keywords:** Boron isotopes, Amorphous Calcium Carbonate (ACC), transformation, pH proxy

## 1. Introduction

The mechanisms controlling the incorporation of boron in carbonate minerals as well as its isotopic fractionation have attracted much attention in the recent literature. This is because the  $\delta^{11}\text{B}$  values of marine calcifiers are commonly used to estimate oceanic paleo-pH. Briefly, the B-isotope pH-proxy is based on the assumption that the aqueous tetragonal borate ion,  $\text{B}(\text{OH})_4^-$ , is incorporated in the crystal lattice of calcite and aragonite and this incorporation is not accompanied by B isotope fractionation (Hemming and Hanson, 1992). The assumption that tetrahedral B is exclusively incorporated in the crystal lattice, however, has been challenged by recent spectroscopic observations of the coexistence of trigonal ( $\text{BO}_3$ ) and tetrahedral ( $\text{BO}_4$ ) boron in both synthetic and marine calcites and aragonites (Sen et al., 1994; Klochko et al., 2009; Rollion-Bard et al., 2011; Mavromatis et al., 2015; Noireaux et al., 2015; Branson et al., 2015). If derived from aqueous trigonal boric acid,  $\text{H}_3\text{BO}_3^0(\text{aq})$ , the presence of  $\text{BO}_3$  in the carbonate lattice complicates the use of the boron isotope composition of carbonates as a pH proxy. At the same time, it should be emphasized that the experimental calibrations of the B pH-proxy are partly based on inorganic calcite and aragonite classical overgrowth experiments, involving ion-by-ion attachment to the crystal advancing steps. A large body of recent literature, however, suggests that many marine calcifiers do not follow this standard growth mechanism, but apply amorphous precursor strategies to build their exoskeletons (e.g. Politi et al., 2004, 2008; Mass et al., 2017; Jacob et al., 2017).

The elementary mechanisms that control the incorporation and isotope fractionation of trace elements in the lattice of calcium carbonates derived from metastable ACC precipitated from highly supersaturated solutions are expected to be different from those operating during standard growth from less supersaturated solutions. A number of studies proposed that ACC transforms to carbonate minerals via a solid-state mechanism, a process that involves dehydration and structural reordering (Lam et al., 2007; Politi et al., 2008; Gong et al. 2012; Bushuev et al., 2015). Conversely, it has been suggested that ACC transformation occurs through a dissolution and re-precipitation reaction (Ogino et al., 1987; Rodriguez-Navarro et al., 2015; Giuffre et al., 2015; Konrad et al., 2018) or through a combination of both processes (Ihli et al., 2014; Nielsen et al., 2014). Understanding which of these processes dominates is important for the interpretation of elemental and isotopic signatures of carbonates. To our knowledge, no prior study until now has monitored the evolution of the boron isotope composition of the forming fluid and the precipitated solid during the formation of Mg-ACC and their subsequent transformation to crystalline calcite or aragonite.

In an effort to characterize the boron isotope fractionation between aqueous solutions and Mg-bearing ACC, as well as during and after the transformation of these amorphous phases to Mg-calcites or aragonite, we measured the B isotope composition of the fluids and formed solids during experimental runs performed under controlled pH conditions that lasted over two years. The mineralogy of the precipitating solids during the course of each run was followed using *in-situ* Raman Spectroscopy, Attenuated Total Reflectance – Fourier Transform Infrared Spectroscopy (ATR-FTIR) and X-ray diffraction whereas the structural status of B in the solids was characterized using  $^{11}\text{B}$  MAS NMR spectroscopy. It is expected that the results of this study will allow for a better understanding of the mechanisms that control B incorporation in carbonate minerals during the non-classical growth pathway that is commonly followed by many marine calcifiers, as well as how this pathway of mineral formation affects B-isotope fractionation between carbonate minerals and the parent fluid.

## 2. Methods

### 2.1 Experimental setup and analytical techniques

The experimental setup and the analytical methods used in this study were described earlier in Purgstaller et al. (2016, 2017a). Briefly, the experiments took place in a temperature controlled ( $25.00 \pm 0.03$  °C) Easy Max<sup>TM</sup> 102 system (Mettler Toledo) equipped with a 150 mL reactor. The formation of boron-bearing Mg-rich ACC was induced by titration at a constant rate (i.e. 2 ml/min) of 50 ml of a 0.6 M (Ca,Mg)Cl<sub>2</sub> solution via an automatic titrator (702 SM Titrino; Methrom) into 50 mL of a solution (stirred at 200 rpm) that contained 1 M NaHCO<sub>3</sub> and ~17 mM B. The pH of the reactive fluid was kept constant by automatic titration of a 1 M NaOH solution (Schott, TitroLine alpha plus). The pH of the experimental solution was measured with a SI Analytics Silamid<sup>®</sup> gel electrode, calibrated against NIST buffer standard solutions at pH 4.01, 7.00 and 10.01 at 25°C. The temporal evolution of mineral precipitation was monitored by in situ Raman spectroscopy (Raman RXN2<sup>TM</sup> analyzer, Kaiser Optical Systems). After 180 min of reaction time, the experimental solution and precipitated solids were transferred into a 150 ml capped, air-tight reactor that was placed on a compact shaker (Edmund Bühler GmbH; KS-15) operating at 150 rpm in a temperature-controlled room at  $25 \pm 1$  °C. The evolution of the chemical and B isotope composition of the experimental fluids and the precipitated solids was followed by homogeneous samplings of the reactor suspension with a pipette at the pre-defined time intervals listed in Table 1. After sampling, the solids were separated from the fluid by vacuum filtration through a 0.2 µm cellulose acetate membrane and were immediately analyzed using Attenuated Total Reflectance-Fourier Transform Infrared Spectroscopy (ATR-FTIR; Perkin Elmer Spektrum 100). The solids were dried in a desiccator containing silica gel at room temperature. The mineralogy of the dried precipitates was determined by X-ray diffraction (PANalytical X'Pert PRO). Aqueous concentrations were measured by inductively coupled plasma optical emission spectrometry (Perkin Elmer Optima

8300 DV) with an analytical error  $< \pm 3\%$  and the total alkalinity of the solutions was determined by HCl titration using an automatic Schott TitroLine alpha plus titrator equipped with a SenTix® 945 pH gel electrode with an analytical precision of  $\pm 2\%$ . The titration endpoint was determined by the first derivative of the pH versus the volume of titrated HCl. In total, 3 experiments were carried out, hereafter called B1, B2 and B3. Their duration was 744 days (Table 1). The initial pH was fixed at 8.8 for experiments B1 and B3, and 8.3 in experiment B2. The initial Mg:Ca ratio of the 0.6 M (Ca,Mg)Cl<sub>2</sub> solution was 1:4 for experiment B1 and B2, and 1:8 for experiment B3. Note that these ratios do not reflect the composition of the reacting fluids and forming solids after the onset of the experimental runs.

Boron speciation in selected solid samples was determined using <sup>11</sup>B ( $I = 3/2$ ) MAS NMR analyses performed at the CEMHTI Laboratory (Orléans, France) using a protocol similar to that described earlier in Mavromatis et al. (2015). Briefly, the <sup>11</sup>B analyses were carried out on a high field Bruker AVANCE III spectrometer (850 MHz–19.9 T), allowing for a complete resolution of the BO<sub>3</sub> and BO<sub>4</sub> contributions. Moreover, the use of a specially designed Doty probe optimized for <sup>11</sup>B signal observation and equipped with a “boron-free” stator ensured the acquisition of spectra that are representative of the sample and free from the probe signal. About 200 mg of solid powder were packed in 3 mm rotors allowing magic angle rotation conditions of 20 kHz. The spectra were acquired at a frequency of 272.8 MHz for <sup>11</sup>B after a short excitation pulse to ensure homogeneous irradiation of boron species. The recycling delay was fixed at 3 s and the number of accumulated scans was adjusted depending on the boron content of the sample. The <sup>11</sup>B chemical shifts were referenced relative to a boron trifluoride diethyl etherate (BF<sub>3</sub>·OEt<sub>2</sub>) solution. The use of a boron-free probe and multiple scans allow the acquisition of reliable spectra for solids with B concentrations as low as 10 ppm. The relative amounts of BO<sub>3</sub> and BO<sub>4</sub> were determined by peak surface integration using the DMfit software (Massiot et al., 2002).

## 2.2 Boron isotope analyses

Prior to boron isotope ratio ( $\delta^{11}\text{B}$ ) measurements, boron was chemically separated from the solid or the solution to obtain a final solution containing only boron in a diluted nitric acid solution ( $\text{HNO}_3=0.05\text{ M}$ ). For solids, 5 mg to 20 mg of the calcium carbonate sample were dissolved in 0.5 M  $\text{HNO}_3$  and ultrasonicated for 30 min in a closed Teflon beaker. An aliquot of the calcium carbonate solution containing 200-500 ng of B was diluted 10 times and the pH brought up to 8-9 with a 4 M distilled ammonium hydroxide solution. For the experimental aqueous solutions, an aliquot containing 200-500 ng of B was diluted 10 times, but as the pH was already in the 8-9 range it did not need adjustment. The sample solutions were subsequently loaded on ion-exchange chromatographic columns that contained 50  $\mu\text{L}$  of the boron-specific Amberlite IRA 743 resin following the protocol by Paris et al. (2010). After washing the columns with 30 mL of 0.5N  $\text{HNO}_3$ , rinsing twice with 0.1 mL of water at pH 9 (addition of ammonia), the sample solutions at pH 8-9 were loaded onto the columns. Boron was retained on the resin whereas the rest of the matrix was discarded. The columns were again rinsed twice with 0.1 mL of water at pH 9. The ion-exchange sites of the resin were saturated with a 2.6 M  $\text{NaNO}_3$  solution at pH 9 and the resin rinsed again with 0.1 mL of water at pH 9. Boron was recovered from the columns with 50  $\mu\text{L}$  of 0.5 N  $\text{HNO}_3$  and with 600  $\mu\text{L}$  of 0.1 N  $\text{HNO}_3$ . The boron solutions were further diluted with 1.05 mL of water to reach a final  $\text{HNO}_3$  concentration of 0.05 N. Blanks for the extraction procedure contained on average  $0.24 \pm 0.17$  ng of B (2SD;  $n=9$ ) and their contribution to the sample  $\delta^{11}\text{B}$  measurement was considered negligible.

Boron isotope ratios were measured on a MC-ICPMS Neptune (Thermo Scientific) at IPGP, using a direct injection nebulizer (d-DIHEN, demountable-Direct Injection High Efficiency Nebulization) connected directly on the torch, following the protocol described by Louvat et al. (2011, 2014). The  $\delta^{11}\text{B}$  values were determined by bracketing with the NIST 951 standard solution (Catanzaro et al., 1970). Each sample solution was measured three times, allowing for the determination of an average and 2SD values. The external reproducibility on

distinct chemical extractions of samples was 0.25‰ (Louvat et al., 2014). Thus, sample  $\delta^{11}\text{B}$  measured with 2SD lower than 0.25‰ were assigned an analytical error of 0.25‰. The accuracy of the  $\delta^{11}\text{B}$  measurements was regularly checked by measuring the standard reference solutions AE120, AE121 and AE122 (Vogl and Rosner, 2011). Long-term average values for these standards are  $-20.31 \pm 0.19$  ‰ (n=16),  $19.58 \pm 0.18$  ‰ (n=59) and  $39.35 \pm 0.21$  ‰ for AE120, AE121 and AE122, respectively (Louvat et al., 2019), in good agreement with the certified values ( $-20.2 \pm 0.6$  ‰,  $19.9 \pm 0.6$  ‰ and  $39.9 \pm 0.6$  ‰, respectively; Vogl and Rosner, 2011).

### 2.3. Speciation calculations

Aqueous speciation of the experimental solutions was calculated using the PHREEQC software together with its MINTEQ.V4 database (Parkhurst and Appelo, 2013) modified by the addition of the solubility products for hydromagnesite (Gautier et al., 2014), nesquehonite and dypingite (Harrison et al., 2019). This model calculates the activity coefficients of free aqueous ions and charged complexes using the Davies equation. The value for the boric acid hydrolysis constant was taken from Baes and Mesmer (1976). The values of the formation constants for  $\text{MgB}(\text{OH})_4^+$  and  $\text{CaB}(\text{OH})_4^+$  ion pairs were taken from the NIST database (Martell et al., 2004), whereas those for the  $\text{NaB}(\text{OH})_4^\circ$  and  $\text{B}(\text{OH})_2\text{CO}_3^-$  ion pairs were taken from Pokrovski et al. (1995) and McElligott and Byrne (1997). The formation constants for these ion pairs are listed in Table A2 of the Electronic Annex. We note that the Davies equation used by the MINTEQ.V4 model is suitable for defining aqueous speciation in dilute solutions ( $I \leq 0.5$ ; Allison et al., 1991). Given that our reactive solutions' ionic strengths ranged between 0.85 and 0.55 M (Table 1), MINTEQ.V4 may not properly define aqueous speciation in our solutions. To address this, we performed speciation calculations using PHREEQC software with the Pitzer ion interaction model. However, Pitzer is also not an ideal candidate for our solutions as this model makes no provision for boron ion pairs with sodium and bicarbonate ions, and thus cannot precisely

describe B coordination in the fluid phase. Our preferred approach is to use the speciation computed with MINTEQA4, as we do throughout this study. For comparison, we also provide aqueous B speciation estimated using the PITZER model in Table A3 of the Electronic Annex.

### 3. Results

#### 3.1 Chemical composition of the experimental fluids and solids

The temporal evolution of the chemical composition of the experimental fluids is depicted in Fig. 1 and the measured concentrations are reported in Table 1. As showed in Fig. 1A, Ca concentrations in the experimental fluids increase during the first 25 min after the onset of the runs, due to the addition of the inlet (Ca,Mg)Cl<sub>2</sub> solution. After the end of the titration of the input solution, however, Ca concentrations in the experimental fluids decrease suddenly from 3-5 mM to less than 0.5 mM after 100 min of reaction. This sharp decrease of the Ca aqueous concentrations and saturation indices with respect to CaCO<sub>3</sub> minerals reflect the transformation of precipitated ACC into crystalline carbonate minerals (see Table 1). As illustrated in Fig. 1B, Mg concentrations in the reactive fluids exhibit a similar behavior to that of Ca during the first 25 min of the experiments. In experiments B2 and B3, the aqueous Mg concentrations decrease exponentially after the end of the titration of the input solution and until the end of the experimental runs. In contrast, in experiment B1, the Mg concentration increased during the first 180 min of reaction up to 45 mM and then exponentially decreased until the end of the experimental run. Note, however, that the final aqueous Mg concentration in the B1 run (9.3 mM) is much higher than the corresponding Mg concentrations in the B2 and B3 runs (0.06-0.3 mM). Aqueous B concentrations in the three experimental runs (Fig. 1C) decrease continuously for the first 25 min, after which they remain nearly constant until the end of the experiments at 6±0.5 mM. It is important to note that B is initially present in the reactor together with the dissolved inorganic carbon, but is absent in the input solution. Hence, the continuous decrease of B concentration within the first 25 min of reaction in all experimental

runs is the result of dilution due to titration of the input solution and not to the weak boron incorporation in the precipitating carbonate solids (see Fig. 1C). This is further supported by the linear correlation between aqueous Na and B concentrations (not shown here).

The precipitation rates (mmol/s) of the forming solid phases were estimated in a similar manner as in Mavromatis et al. (2017b), based on the mass balance of the Ca and Mg introduced by the titration of the input (Ca,Mg)Cl<sub>2</sub> solution and the actual aqueous Ca and Mg concentrations in the reactor according to:

$$r_p = \frac{Ca_{add} + Mg_{add} - Ca_{meas} - Mg_{meas}}{t} \quad (1)$$

where the subscripts  $X_{add}$  and  $X_{meas}$  denote the number of moles of Ca or Mg added and measured in the reactor, respectively, and  $t$  is the elapsed reaction time in seconds from the onset of the experimental runs. The temporal evolution of the carbonate precipitation rates is illustrated in Fig. 2a. It can be seen that they decrease sharply with time from 0.27-0.30 mmol/s at the onset of precipitation to < 0.01 mmol/s after 1000 min of reaction time. To allow their comparison with literature rates generally expressed in mol/m<sup>2</sup>/s, the rates estimated in the present study were recalculated assuming a specific BET surface area of the precipitated ACC and Mg-calcite/aragonite of ~50 m<sup>2</sup>/g (Rahda and Natrovsky, 2015). The results reported in Fig. 2B show that precipitation rates drop from 3×10<sup>-6</sup> mol/m<sup>2</sup>/s at the beginning of titration to <10<sup>-8</sup> mol/m<sup>2</sup>/s after 1000 min (0.7 days) of reaction.

### 3.2 Mineralogy and chemical composition of the forming solids

The temporal evolution of the mineralogy of the solid phases is presented in Table 1. At the onset of all the experimental runs, *in-situ* Raman spectroscopy reveals the presence of Mg-ACC that is identified by a broad carbonate symmetric stretching band ( $\nu_1$ ) at 1080–1088 cm<sup>-1</sup> and the absence of lattice modes (libration and translation mode) at lower frequencies (see Purgstaller et al., 2017b; 2019). The formation of Mg-ACC is further confirmed by the ATR-FTIR spectra of solids recorded shortly after sampling (Fig. 3). These spectra are characterized

by the absence of the  $\nu_4$  absorption band at  $713\text{ cm}^{-1}$  that is diagnostic of calcite, and the presence of broad  $\nu_1$  and  $\nu_2$  bands at  $1073\text{--}1075\text{ cm}^{-1}$  and  $860\text{--}861\text{ cm}^{-1}$ , respectively (Fig. 3) that are indicative of Mg-ACC. The presence of Mg-ACC was detected for up to 60, 40 and 30 min of reaction time for experiments B1, B2 and B3 respectively (Table 1). After longer reaction times, the Mg-ACC transformed to a crystalline carbonate mineral.

In experiment B1, after 100 min of reaction, the mineral in contact with the experimental fluid was monohydrocalcite (Fig. 3). In the sample taken after 1 day of reaction, additional X-ray diffraction peaks corresponding to hydromagnesite were identified. The co-existence of the two mineral phases in experiment B1 lasted up to 14 days of reaction time with hydromagnesite representing less than 5 wt % of the total solid mass. ATR-FTIR spectra and XRD patterns show that, after 46 days of reaction, the recovered solids consisted mainly of aragonite with minor amounts of calcite ( $\sim 1\%$ ) and hydromagnesite (Table 1, Fig. 3). Over time the abundance of hydromagnesite in the solid phase remained constant at  $\sim 4\text{ wt. \%}$  except for the last sample where it increased up to  $9\text{ wt. \%}$  (Table 1). This last feature is consistent with the overall decrease of the aqueous Mg and alkalinity concentrations and the abrupt pH increase in the last sample (see Fig. 1B and Table 1).

In experiment B2, the initially formed Mg-rich ACC transformed, after 40-50 minutes, into Mg-rich calcite, the only mineral identified until the end of the experimental run (Fig. 3). As revealed by XRD and chemical analyses of the solids, the Mg content of the Mg-calcite increased from  $\sim 12\text{ mol \%}$  after 40-50 minutes of reaction to  $\sim 19\text{ mol \%}$  at the end of the experimental run. This is consistent with the overall decrease of the aqueous Mg and alkalinity concentrations (see Fig. 3 and Table 1). Like in experiment B2, in experiment B3, Mg-rich ACC transformed to a Mg-rich calcite after 25-40 minutes of reaction, the only mineral phase detected until the end of the experimental run (Fig. 3). Note that in this experiment there was a net increase of the Mg content of the solid from 7 to  $\sim 11\text{ mol\%}$  between 25 min and 744 days of reaction.

Characteristic scanning electron microphotographs of the solid material recovered from the reactors after Mg-ACC transformation are shown in Fig. 4. In experiment B1, the recovered monohydrocalcite consists of aggregates of spherical particles a few nm in diameter (Fig. 4A) that increase in size over time (see Fig. 4B). The aragonite crystals recovered at the end of the run exhibit a pseudo-hexagonal form (Fig. 4C-D), similar to the aragonite crystals reported by Purgstaller et al. (2017b). These crystals do not increase in size between 546 and 744 days of experimental run, as seen in Figs. 4C and 4D. Note that the hydromagnesite that occurs together with monohydrocalcite and aragonite exhibits a plate-like morphology (Fig. 4B-D). In the experiments B2 and B3, the Mg-calcite solids collected at the end of the runs consist of aggregates of aligned, submicron-sized, rhombohedral crystals, which is typical of ACC derived Mg-calcites (Loste et al., 2003; Mavromatis et al., 2012; Purgstaller et al., 2016). No significant variations in the shape and size of the Mg-calcite aggregates in experiments B2 and B3 can be seen after 744 days of experimental run (Figs. 4E and 4F), an observation that is consistent with the mineralogy of the crystals remaining the same until the end of the runs B2 and B3.

### 3.3 Boron partition coefficient between the solid phases and the fluids.

The boron concentration in the solid phase reaches a maximum value of  $\sim 500 \pm 100$  mg/kg when Mg-ACC is formed. During the progressive transformation of Mg-ACC into crystalline carbonates, B concentrations decrease to  $200 \pm 50$  mg/kg after 1440 min of reaction in all experimental runs. The boron partition coefficient,  $D_B$ , between  $\text{CaCO}_3$  and the aqueous solution was calculated as in Mavromatis et al. (2015) according to:

$$D_B = \frac{(X_B)_{\text{CaCO}_3}}{([B_T]/[CO_3^{2-}])_{\text{fluid}}} \quad (2)$$

where  $X_B$  denotes the mole fraction of B in the precipitated solid whereas  $[B_T]$  and  $[CO_3^{2-}]$  are the molalities of total boron and the carbonate ion in the fluid phase, respectively. Note that Eq.

(2) assumes an ideal substitution of boron, either as  $B(OH)_3^0$  or  $B(OH)_4^-$  for  $CO_3^{2-}$  ions in the solid phase.  $D_B$  values are listed in Table 1 and plotted as function of reaction time in Fig. 5. The  $D_B$  value corresponding to ACC precipitation is equal to  $10^{-2.15 \pm 0.1}$ . This value is 2.5-4.0 orders of magnitude higher than those reported in Mavromatis et al. (2015) for the classical nucleation/growth of calcite and/or aragonite. During the transformation of ACC into crystalline material,  $D_B$  decreased significantly, achieving values equal to  $10^{-2.85}$ ,  $10^{-2.9}$  and  $10^{-3.6}$  in runs B1 (pH ~8.8), B3 (pH ~8.8) and B2 (pH ~8.3), respectively, after 744 days of reaction.

### 3.4 Boron speciation and isotope composition in the fluid and solid phases

The aqueous boron speciation in the experimental fluids can be found in Table A1 of the Electronic Annex. At the onset of the titration of the 0.6 M (Ca,Mg)Cl<sub>2</sub> into the NaHCO<sub>3</sub> solution, B aqueous speciation is dominated at pH 8.8 and 8.3 by  $B(OH)_2CO_3^-$  which accounts for 30 to 50 % of the total boron after 5 minutes of reaction. As the titration proceeds and alkalinity decreases, the fraction of this ion pair diminishes and accounts for only 7 to 14% of the total boron at the end of the titration. After 25 minutes of reaction, the major boron aqueous species at pH ~ 8.8 (i.e exp. B1 and B3) are boric acid ( $H_3BO_3^0$ ), the borate ion ( $B(OH)_4^-$ ) and the sodium-borate ion pair ( $NaH_2BO_3^0$ ) whose relative contributions to the total boron concentration average  $38 \pm 10\%$ ,  $42 \pm 9\%$ , and  $15 \pm 3\%$ , respectively. At pH~ 8.3 (i.e. exp. B2), the corresponding abundances are  $68 \pm 4\%$ ,  $14 \pm 3\%$  and  $5 \pm 1\%$ . Note that the last sample of experiment B1 exhibits an increase in pH of about 0.6 units which induces a significant decrease in the calculated fraction of boric acid. Similarly, in experiment B3 (pH ~ 8.8), the pH of the experimental fluid increased to ~9.0 after 1 day of reaction, resulting in an increase of the relative abundance of the aqueous  $B(OH)_4^-$  species.

The coordination of boron species in selected precipitated solids is reported in Table 2 whereas the <sup>11</sup>B NMR spectra can be seen in Figs. A1-A3 of the Electronic Annex. Boron coordination does not exhibit significant temporal variations, with tetrahedral BO<sub>4</sub> accounting

for 36-46%, 34-46% and 46-57% of the total boron in solids formed during experiments B1, B2 and B3, respectively. It is worth noting that boron coordination in precipitated Mg-ACC seems to depend only slightly on the solution pH. At the end of the titration (25 min),  $\text{BO}_4$  in the precipitated Mg-ACC accounts for ~46-50 % of the total solid boron in all three experiments (see Figs. A1-A3). However, whereas at pH = 8.8 there is a fair agreement between the relative abundances of  $\text{BO}_4$  in the solids and experimental solution, at pH = 8.3 the fraction of  $\text{BO}_4$  in ACC and Mg calcite (~ 40-50%) is much higher than the calculated fraction of aqueous  $\text{B}(\text{OH})_4^-$  species (26%). The transformation of ACC to calcite and aragonite was not accompanied by measurable changes in the distribution of  $\text{BO}_3$  and  $\text{BO}_4$  in the solids and aragonite was not enriched in  $\text{BO}_4$  compared to calcite. Note, however, that the solids collected at the end of the runs were significantly enriched in  $\text{BO}_4$ .

The  $\delta^{11}\text{B}$  compositions of the experimental fluids and bulk solids are reported in Table 2 and depicted as a function of time in Fig. 6A and 6B. During the titration, the aqueous B in the reactor becomes progressively enriched in  $^{11}\text{B}$ , with  $\delta^{11}\text{B}_{\text{fluid}}$  increasing from -0.29 ‰ up to + 4 ‰ at the end of the titration in experiment B1. At the end of the titration, there is a reversal in the temporal evolution of the aqueous B isotope composition with a sharp initial decrease of  $\delta^{11}\text{B}_{\text{fluid}}$  values followed by the attainment of a steady-state at  $0.5 \pm 0.5$  ‰ after about 3 days (~3400 min) of reaction. The evolution of the isotope composition of precipitated solids mirrors that of the aqueous boron. During the initial titration, the solids become progressively depleted in  $^{11}\text{B}$ , with  $\delta^{11}\text{B}_{\text{solid}}$  values of -9.5 and -13.3 ‰ in runs B1 and B2, respectively, but no change was observed in run B3. It should be noted that, until the end of the titration (25 min), Mg-ACC are the only solid phases precipitating in the reactor. At the end of the titration, the trend reverses and  $\delta^{11}\text{B}_{\text{solid}}$  values increase with time until attainment of a quasi-steady state after about 7 days (~ $10^4$  min) of reaction. The  $\delta^{11}\text{B}$  composition of the solids collected at the end of the runs depends on their mineralogy and the fluid pH:  $-4.0 \pm 2.0$  ‰ (aragonite, pH=8.8, B1),  $-7.6 \pm 1.2$  ‰ (calcite, pH=8.8, B3),  $-11.0 \pm 1.5$  ‰ (calcite, pH=8.3, B2).

### 3.5 Boron isotope fractionation between the solid and the fluid

Boron isotope fractionation between the solid and experimental fluid can be expressed as:

$$\Delta^{11}\text{B}_{\text{solid-fluid}} = \delta^{11}\text{B}_{\text{solid}} - \delta^{11}\text{B}_{\text{fluid}} \quad (3)$$

The temporal evolution of  $\Delta^{11}\text{B}_{\text{solid-fluid}}$  is presented in Fig. 6E and 6F. The same temporal evolution of  $\Delta^{11}\text{B}_{\text{solid-fluid}}$  is observed in the three experimental runs with a depletion of the solids in  $^{11}\text{B}$  at the onset of Mg-ACC precipitation followed by an increase of the extent of fractionation during the titration period. The  $\Delta^{11}\text{B}_{\text{solid-fluid}}$  values obtained after 5 min are  $-8.3 \pm 1.4$  ‰ and they decrease to  $-14 \pm 2.0$  ‰ after 25 min. After the titration, the extent of isotope fractionation progressively decreased with time until attainment of a quasi steady-state after about 3 days of reaction ( $\sim 10^3$  min). The  $\Delta^{11}\text{B}_{\text{solid-fluid}}$  values at steady state were  $-4.0 \pm 1.5$  ‰,  $-11.0 \pm 1.5$  ‰ and  $-7.5 \pm 1.2$  ‰, for experiments B1 (pH 8.8), B2 (pH 8.3) and B3 (pH 8.8), respectively.

To exclude the effect of pH and aqueous B speciation on the fractionation factor, it is useful to express the fractionation factor with respect to the isotope composition of the aqueous borate ion ( $\Delta^{11}\text{B}_{\text{solid-B4}} = \delta^{11}\text{B}_{\text{solid}} - \delta^{11}\text{B}_{\text{B4}}$ ) instead of that of the fluid ( $\Delta^{11}\text{B}_{\text{solid-fluid}} = \delta^{11}\text{B}_{\text{solid}} - \delta^{11}\text{B}_{\text{fluid}}$ ). For this purpose, the isotope composition of the borate ion, including borate ion aquo-complexes was estimated as in Nir et al. (2015) according to:

$$\delta^{11}\text{B}_4 = \frac{\delta^{11}\text{B}_T - \varepsilon_B B_3}{\alpha_B B_3 - (1 - B_3)} \quad (4)$$

where  $\delta^{11}\text{B}_T$  denotes the boron isotope composition of the fluid,  $\varepsilon_B$  is the fractionation between boric acid and the borate ion in ‰,  $\alpha_B = (10^{-3}\varepsilon_B + 1)$  is the fractionation factor between the same species, and  $B_3$  is the fraction of boric acid in the aqueous phase. The  $\varepsilon_B$  value of 26 ‰ taken from Nir et al. (2015) was used in these calculations. Calculated values of  $\Delta^{11}\text{B}_{\text{solid-B4}}$  are listed in Table 2 and their temporal evolution in our experiments is illustrated in Fig. 7. Unlike

$\Delta^{11}\text{B}_{\text{solid-fluid}}$ ,  $\Delta^{11}\text{B}_{\text{solid-B4}}$  is generally positive, reflecting solids enriched in  $^{11}\text{B}$  with respect to the aqueous borate. The temporal evolution of  $\Delta^{11}\text{B}_{\text{solid-B4}}$  mirrors that of  $\Delta^{11}\text{B}_{\text{solid-fluid}}$  with a marked decrease of the extent of fractionation during the titration period and the precipitation of Mg-ACC followed, after the titration, by a rapid increase of fractionation and attainment of a steady-state after a few days of reaction. At the end of the runs,  $\Delta^{11}\text{B}_{\text{solid-B4}}$  values are equal to  $6.8 \pm 1.3 \text{ ‰}$ ,  $7.1 \pm 1.6 \text{ ‰}$  and  $-0.8 \pm 2.9 \text{ ‰}$  for B1 (aragonite, pH 8.8), B2 (calcite, pH 8.3) and B3 (calcite, pH 8.9), respectively. Note that using the theoretical value of  $\varepsilon_B$  proposed by Balan et al. (2018;  $\varepsilon_B = 32.7\text{‰}$ ) yields  $\Delta^{11}\text{B}_{\text{solid-B4}}$  values for experiments B1 (aragonite), B2 (calcite, pH=8.3) and B3 (calcite, pH=8.9) of  $9.6 \pm 1.4$ ,  $11.7 \pm 1.7$  and  $1.1 \pm 3.5$ , respectively.

## 4. Discussion

### 4.1 Boron distribution coefficient between the solid and reactive fluid

As it can be seen in Fig. 5, the  $D_B$  value corresponding to ACC precipitation is equal to  $10^{-2.25 \pm 0.2}$ . This value is similar for all the experimental runs despite the different pH values of runs B1 and B3 (8.8) and B2 (8.3). It is significantly higher than corresponding values reported earlier for inorganic calcite and aragonite at the same fluid pH (see Fig. 8A), being 1.5-4.0 orders of magnitude higher than those reported in Mavromatis et al. (2015), Uchikawa et al. (2015) and Kaczmarek et al. (2016) for the classical nucleation/growth of calcite. A similar increase in  $D_B$  values is observed when comparing ACC precipitated in this study and aragonite formed during classical growth (Mavromatis et al., 2015). This value is also  $\sim 2$  orders of magnitude greater than those reported by Allen et al. (2011) for culture experiments with planktic foraminifera *Orbulina universa*. It is likely that the high  $D_B$  values of ACC are affected by the entrapped fluid in the porous network structure of the solid phase. The high  $D_B$  values of ACC are an indication of the presence of two distinct boron reservoirs in Mg-ACC and/or the higher incorporation of B in the amorphous solid.

After the transformation of ACC into crystalline solids,  $D_B$  values decrease significantly but, after two years of solid-fluid interactions, measured  $D_B$  values do not evolve to the levels reported in the literature, being one to two orders of magnitude greater than for inorganic standard crystal growth and one order of magnitude greater than in cultured foraminifera (Fig. 8A). However, it should be noted that the parent fluid  $\text{CO}_3^{2-}(\text{aq})$  concentrations in the present experiments are about one to four orders of magnitude higher than in the previous studies (including planktonic foraminifera cultures). In fact, a strong linear correlation is observed between  $\text{Log}D_B$  and  $\text{Log}[\text{CO}_3^{2-}(\text{aq})]$  that can be described as  $\text{Log}D_B = 1.44 \times \text{Log}[\text{CO}_3^{2-}(\text{aq})] - 8.00$ ;  $R^2 = 0.8$ , with  $\text{Log}D_B$  increasing from -6.5 to -2.2 when  $[\text{CO}_3^{2-}(\text{aq})]$  increases from  $10$  to  $2 \times 10^4 \mu\text{mol/kg}$  (Fig. 8B). The linear correlation of Fig. 8B vanishes if the borate concentration, rather than the total boron concentration, is used to compute the  $D_B$  value (not shown). Interestingly, a linear, but weaker, correlation between  $\text{Log}D_B$  and  $\text{Log}[\text{HCO}_3^-(\text{aq})]$  is also observed when  $D_B$  is expressed as a function of  $[\text{HCO}_3^-(\text{aq})]$  rather than  $[\text{CO}_3^{2-}(\text{aq})]$  where  $\text{Log}D_B = 1.43 \times \text{Log}[\text{HCO}_3^-(\text{aq})] - 8.68$ ;  $R^2 = 0.53$  (Fig. A4).

These observations strongly suggest that both  $\text{CO}_3^{2-}(\text{aq})$  and  $\text{HCO}_3^-(\text{aq})$  are involved in boron uptake by the solid. The involvement of  $\text{HCO}_3^-(\text{aq})$  likely occurs at the onset of precipitation. At this time  $\text{B}(\text{OH})_2\text{CO}_3^-$  ion pairs represent up to  $\sim 50\%$  of dissolved boron and could be directly incorporated in the precipitating ACC and/or its entrapped fluid owing to their same charge as  $\text{HCO}_3^-(\text{aq})$ . In addition, the strong correlation between  $D_B$  expressed as a function of total aqueous B and  $\text{CO}_3^{2-}$  concentrations reflects involvement of both  $\text{H}_3\text{BO}_3^\circ(\text{aq})$  and  $\text{B}(\text{OH})_4^-$  during B incorporation. This is in accord with  $^{11}\text{B}$  MAS NMR spectra of the solids (Figs A1-A3), assuming that most trigonal B present in the solid was not derived from the re-coordination of initially incorporated  $\text{BO}_4$ . This suggests that B incorporation in calcite and aragonite, especially during the formation of ACC precursors, involves complex mechanisms and cannot be described by a simple  $\text{B}(\text{OH})_4^- - \text{CO}_3^{2-}$  exchange reaction (Balan et al., 2016). The distinct B speciation in calcite and aragonite resulting from different B incorporation

pathways (see Balan et al., 2016) prevents the definition of a single equilibrium thermodynamic partition coefficient for the two minerals. In addition to the fast kinetics of ACC formation at the onset of the titration ( $\text{Log}r_p > -6.5$  (mol/m<sup>2</sup>/s) during the first 10 min) that leads to kinetic fractionation and indiscriminate incorporation of foreign ions, the fluid composition, including  $\text{HCO}_3^-$ ,  $\text{CO}_3^{2-}$ ,  $\text{Na}^+$ ,  $\text{Ca}^{2+}$ ,  $\text{Mg}^{2+}$  and pH, could strongly affect the final  $D_B$  values even after nearly two years of contact of the solids with the experimental solutions.

#### 4.2 Boron isotope fractionation between amorphous calcium carbonate and the fluid

The Mg-ACC solids that precipitated initially exhibit a small and variable enrichment in <sup>11</sup>B (i.e.  $-6.9 \leq \Delta^{11}\text{B}_{\text{solid-fluid}} \leq -9.8$  ‰; Fig. 6E and 6F) compared to the solids sampled after 25 min of titration and to calcites formed in the same pH range via a classical nucleation/growth mechanism ( $-13 \text{ ‰} \leq \Delta^{11}\text{B}_{\text{solid-fluid}} \leq -16 \text{ ‰}$ ; Noireaux et al., 2015; Farmer et al., 2019). As the titration proceeds, however,  $\Delta^{11}\text{B}_{\text{solid-fluid}}$  progressively becomes more negative, exhibiting values of  $-12.1 \leq \Delta^{11}\text{B}_{\text{solid-fluid}} \leq -15.9$  ‰ at the end of titration. The small initial isotope discrimination could be explained by the presence of B in two distinct reservoirs, the amorphous solid and its porous hydrated network (Bushuev et al., 2015). Aqueous boron chemical and isotope compositions in the interconnected channels of the amorphous solid are assumed to reflect that of the bulk fluid ( $[\text{B}_{\text{aq}}] \sim 16$  mmol/L,  $\delta^{11}\text{B}_{\text{initial-fluid}} = -0.29$  ‰). The subsequent and progressive depletion of the solids in <sup>11</sup>B until the end of the titration (see Fig. 6C and 6D), together with the decrease of B solid concentration (Table 1), likely reflects a weaker contribution with time of pore-channels B to the overall Mg-ACC boron content and isotope composition. This would result from the partial dehydration of ACC, which has been shown to occur in solution before crystallization of more stable phases (e.g. Rodriguez-Navarro et al., 2015).

### 4.3 Boron isotope fractionation between carbonate minerals and the fluid

Shortly after the end of the titration of the (Ca,Mg)Cl<sub>2</sub> solution, precipitated Mg-rich ACC undergoes transformation into crystalline phases. The transformation is accompanied by a change of the bulk  $\delta^{11}\text{B}_{\text{solid}}$  in all experiments, together with an evolution of the mineralogy in experiment B1 and an increase of the Mg concentration in calcite formed in experiments B2 and B3. Notably, in experiments B2 and B3, X-ray diffraction patterns reveal the presence of a single mineral phase, suggesting incorporation of Mg derived from the aqueous phase to calcite but not the formation of a distinct Mg-carbonate phase. Moreover, the B content of the solids continuously decreased over time (see Table 1), and their  $\delta^{11}\text{B}$ , after a rapid increase, reached a quasi steady-state (within  $\pm 1.5\%$ ) within a few days (Fig. 6C-D). These observations suggest that the transformation of the amorphous solid to crystalline material proceeds via a dissolution and re-precipitation process during which a continuous exchange of ions between the solid and the experimental fluid occurs (Rodriguez-Navarro et al., 2015), initially at significantly reduced mineral growth rates ( $\sim 10^{-7}$  mol/m<sup>2</sup>/s) and, after 1000 min, at extremely low growth rates ( $< 10^{-9}$  mol/m<sup>2</sup>/s) as equilibrium conditions are approached.

During the crystallization process, the BO<sub>3</sub>/BO<sub>4</sub> in the solids remains relatively constant with about 60 and 45 % BO<sub>3</sub> at pH 8.3 and 8.85, respectively (Figs. A1 to A3). The near-equilibrium solid-fluid ion exchange process is favoured by the transformation of Mg-ACC into nano-crystals of high surface area (see Fig 4D-F). This continuous solid-fluid exchange leads to the achievement of an apparent isotopic steady-state. Note that in the case of experiments B2 and B3, Mg-ACC transforms directly to Mg-calcite, whereas in experiment B1 Mg-ACC initially crystallizes into nano-crystalline monohydrocalcite (Fig. 4A-B) before transforming to nano-crystalline aragonite (Fig. 4C-D). It has been argued that element exchange between carbonate solids and reacting fluids under near-equilibrium conditions leads not only to chemical but also isotopic equilibrium, with the latter being achieved at a slower rate (Pearce et al., 2012; Mavromatis et al. 2016; 2017a; Oelkers et al., 2019). Within this framework it can

be argued that calcite or aragonite, formed via an amorphous precursor, are likely to reach isotope equilibrium, as reported for Mg and O isotopes in studies using an experimental protocol similar to the present one (i.e. Mavromatis et al., 2017b; Dietzel et al., 2020). Nevertheless, it should be noted, as discussed above (see § 4.1), that the exact mechanisms controlling the exchange between solid  $\text{CO}_3$  and aqueous  $\text{H}_3\text{BO}_3^0$  -  $\text{B}(\text{OH})_4^-$  are complex and poorly known. Accordingly, the observation of constant values of  $D_B$  as defined by Eq. 2 is not proof of achievement of equilibrium B partitioning and isotope fractionation. The steady-state B-isotope fractionation determined in this study for Mg-ACC-derived aragonite and calcite can be compared to those measured in previous studies where  $\text{CaCO}_3$  formed via a classical growth mechanism (e.g. Noireaux et al., 2015; Kaczmarek et al., 2016; Farmer et al. 2019), and to the equilibrium fractionation factor values based on first principle calculations (Balan et al., 2018). For this purpose, we compared the B isotope fractionation between the solid and aqueous borate according to Eq. (4).

*Aragonite:* The  $\Delta^{11}\text{B}_{\text{aragonite-B4}}$  value of  $6.7 \pm 1.3$  ‰ (n=3; t=46-649 days) determined at steady-state in the present study (exp. B1) is in good agreement with the ab-initio estimates of Balan et al. (2018) who proposed an equilibrium value between structural  $\text{B}(\text{OH})_4^-$  in aragonite and  $\text{B}(\text{OH})_4^-$  (aq) of  $\sim 10.8$ ‰ (Fig. 7A). Note that the value of  $\alpha_B$  computed by Balan et al. (2018) is equal to 1.0327, whereas the value used in the present study is 1.026 (Nir et al., 2015). Using an  $\alpha_B$  of 1.0327 yields a  $\Delta^{11}\text{B}_{\text{aragonite-B4}}$  of  $9.6 \pm 1.4$  ‰. Interestingly, however, the measured  $\Delta^{11}\text{B}_{\text{aragonite-B4}}$  value reflects a significant enrichment of the solid in  $^{11}\text{B}$  and contrasts with the value determined by Noireaux et al. (2015) for aragonite. These authors reported a value of  $\Delta^{11}\text{B}_{\text{aragonite-B4}} \sim 0$  ‰ for aragonite classical growth implying no fractionation between solid B and aqueous borate. In addition, whereas  $> 90$  % of the boron co-precipitated with aragonite in the Noireaux et al. (2015) study was in tetrahedral coordination, in the present work only 40-50 % of the B is tetrahedrally coordinated.

The contrasting B isotope fractionation observed in the present study and in the Noireaux et al. (2015) could be explained by the differential pathways of aragonite nucleation/growth in the two studies, as illustrated in Fig. 9. In the classical growth pathway operating in Noireaux et al. (2015) experiments, B is attached as a tetrahedral borate complex to aragonite advancing steps with insignificant isotope fractionation relative to the borate ion (Saldi et al., 2018). The incorporation of adsorbed boron in the aragonite lattice proceeds without exchange with the fluid and thus without a change in B solid speciation (see NMR spectra of Fig. 9) or isotope composition. This formation pathway does not lead to isotope equilibrium as computed by the ab-initio calculations of Balan et al. (2018;  $\Delta^{11}\text{B}_{\text{aragonite-B4}} = 10.8$  ‰). The transient amorphous precursors formed in this study at the onset of titration are likely affected by kinetic effects because of their fast formation rates ( $\text{Log}r_p \geq 6.2$  (mol/m<sup>2</sup>/s for  $t \leq 10$  min). For comparable rates of CaCO<sub>3</sub> classical growth, kinetic isotope fractionation of B in calcite (Farmer et al., 2019) and kinetic isotope fractionation of Ba and Sr in aragonite (Mavromatis et al., 2020; AlKhatib and Eisenhauer, 2017) have been observed and can be explained within the framework of the surface kinetic model (DePaolo, 2011). However, in this study, the progressive transformation of ACC into monohydrocalcite and then to aragonite during the following 740 days proceeded via dissolution-precipitation reactions that occurred at very low rates ( $r_p < 10^{-9}$  mol/m<sup>2</sup>/s for  $t > 1000$  min). The subsequent evolution of the  $\delta^{11}\text{B}_{\text{solid}}$  thus occurred under near chemical equilibrium conditions and it can be expected that initial kinetic signatures were erased. Despite the good agreement between calculated steady-state and theoretical  $\Delta^{11}\text{B}_{\text{aragonite-B4}}$  values, it cannot be excluded, however, that these values may be influenced by the complex mechanisms controlling boron incorporation in ACC-derived carbonate minerals.

*Mg-Calcite*. The calcite formed in experiment B2 at pH ~8.3 exhibits at steady-state a  $\Delta^{11}\text{B}_{\text{calcite-B4}}$  value of  $7.1 \pm 1.6$ ‰. This value is in good agreement with the experimental results obtained during calcite classical growth at the same pH by Noireaux et al. (2015; i.e. ~

8 ‰) and Farmer et al. (2019; i.e. ~ 6-7 ‰). Moreover, when calculated with a  $\alpha_B$  value of 1.0327 the  $\Delta^{11}\text{B}_{\text{calcite-B4}}$  becomes  $\sim 11.7 \pm 1.7\%$  and is in excellent agreement with the theoretical estimate of Balan et al. (2018) who proposed a value of  $\sim 13.4\%$  (Fig. 7B). For experiment B3 conducted at pH  $\sim 9.0$ , the resulting  $\Delta^{11}\text{B}_{\text{solid-B4}}$  value is  $\sim -0.8 \pm 2.9\%$ , suggesting that the calcite isotope composition is similar to that of  $\text{B}(\text{OH})_4^-(\text{aq})$ . This value is in good agreement with the results obtained at pH 8.8 by Kazmarek et al. (2016; i.e.  $0 \pm 1\%$ ) and of Noireaux et al. (2015; i.e. 4 ‰ at pH 8.9) but contrasts with the ab-initio estimates of  $\sim 13.4\%$  by Balan et al. (2018). This apparent absence of fractionation could result from faster precipitation kinetics and thus a greater preference for borate incorporation in the calcite lattice (Farmer et al., 2019) and/or a change of the  $\text{B}(\text{OH})_4^-$  local environment at pH  $> 8.5$  (Balan et al., 2018).

Given the general good agreement of the results of this study with the ab-initio calculations of isotope fractionation between tetragonal B in aragonite and calcite and aqueous borate, it can be inferred that the exact proportion of the  $\text{BO}_3$  and  $\text{BO}_4$  in  $\text{CaCO}_3$  has little effect on the B isotope composition. The calcium carbonate mineral thus appears to retain the isotope composition of the incorporated borate ion even if a fraction of it is later de-hydroxylated to trigonal  $\text{BO}_3^{3-}$  (Noireaux et al., 2015; Branson et al., 2015). Nevertheless, in contrast to the previous working hypotheses (Hemming and Hanson, 1992; Hemming et al., 1995; Noireaux et al., 2015; Branson et al., 2015), results of this study and of ab-initio calculations (Balan et al., 2018) suggest that there is a significant fractionation between the aqueous borate ion and  $\text{BO}_3\text{-BO}_4$  in the solid phase. The lack of isotope fractionation between the borate ion in the solid phase and aqueous borate reported during the  $\text{CaCO}_3$  classical growth (Noireaux et al., 2015) could indicate an out-of-equilibrium B incorporation in the crystal without noticeable fractionation, following a local equilibrium of the solution with adsorbed borate species displaying a small fractionation relative to aqueous borate (Saldi et al., 2018). Such an out-of-

equilibrium step may not occur during a non-classical  $\text{CaCO}_3$  formation pathway where the transformation of ACC precursors into stable crystalline phase proceeds via continuous dissolution/precipitation of the solids under near-equilibrium conditions.

#### 4.4 Implications for the interpretation of chemical and isotope composition of natural carbonate minerals formed via an amorphous precursor

Boron-isotope ratios of marine carbonates have been used in numerous studies as a proxy to reconstruct the oceanic paleo-pH (e.g. Hönisch and Hemming, 2005; Foster, 2008; Douville et al., 2010; Rae et al., 2011). The boron pH-proxy assumes the preferential incorporation of  $\text{B(OH)}_4^-$ (aq) in the precipitating  $\text{CaCO}_3$  minerals (Hemming and Hanson, 1992), yet enrichment in  $^{11}\text{B}$  relative to the expected  $\delta^{11}\text{B}$  values of  $\text{B(OH)}_4^-$  has been observed in biogenic carbonates produced in pH-controlled culture experiments. This effect has been interpreted as a pH modification within the calcification microenvironment (e.g. Hönisch et al., 2003; Rollion-Bard and Erez, 2010) or as additional incorporation of aqueous  $\text{H}_3\text{BO}_3^\circ$  (Uchikawa et al., 2015; Noireaux et al., 2015). It has been argued, however, that marine calcifiers, such as foraminifera (Jacob et al., 2017), bivalve shells (Jacob et al., 2011) and corals (Mass et al., 2017) form from an amorphous precursor during calcification processes. The results of this study offer an alternative explanation of the offset that has been observed between the  $\delta^{11}\text{B}$  values of marine biogenic  $\text{CaCO}_3$  and that of seawater  $\text{B(OH)}_4^-$ . They suggest that during non-classical growth of calcite and aragonite, the B-isotope composition of the mineral phase is likely to correspond to that estimated by ab-initio calculations. Note that this does not hold true for calcite formed at pH~8.9, suggesting that changes in aqueous speciation under elevated pH conditions (see above) may be responsible for slight changes of the calcite  $\text{BO}_4$  environment and isotope composition.

It is likely that the ACC pathway of carbonate formation can explain the specific calibration of the B pH-proxy that is recorded in cultured foraminifera and corals (e.g., Trotter et al., 2011; Henehan et al., 2013). Note, however, that our results provide only an indication of the mechanisms that control the B isotope composition of CaCO<sub>3</sub> minerals formed through an amorphous precursor, and additional work over a wider pH range as well as in environments similar to those encountered during biomineralization is required. Moreover, future work would benefit from experimental conditions where ionic strength can remain quasi constant during the experimental runs and the transformation rate of the amorphous solid to crystalline material can be better constrained using a protocol such as the one described in Goetschl et al. (2021).

## 5. Conclusions

In this study, we investigated the B chemical and isotope composition of Mg-calcite and aragonite formed from the transformation of an amorphous precursor phase in experimental runs that lasted ~2 years. The results suggest that the B content of the solid phase, expressed as a partitioning coefficient, is at least 2 orders of magnitude higher in the products of this study than in calcites and aragonites formed inorganically through the classical mineral growth mechanism. It is notable that the B content of the solid remains high after the transformation of the amorphous phase to a crystalline calcium carbonate as it proceeds via dissolution and reprecipitation from the aqueous phase at very slow rates.

The higher concentration of HCO<sub>3</sub><sup>-</sup>(aq) and CO<sub>3</sub><sup>2-</sup>(aq) in the experimental fluids of the present work compared to previous studies, together with the strong correlation observed between B partition coefficients and aqueous carbonate concentrations, strongly suggest that CO<sub>3</sub><sup>2-</sup>(aq), HCO<sub>3</sub><sup>-</sup>(aq) and the B(OH)<sub>2</sub>CO<sub>3</sub><sup>-</sup> aqueous complex are involved in B incorporation in the carbonate lattice. The mechanisms of B partitioning between the fluid and CaCO<sub>3</sub> are thus more complex than is traditionally thought.

The B isotope composition of calcite and aragonite suggests that there is a significant isotope fractionation between aqueous borate and  $\text{BO}_4$  in the solid phase. This observation is consistent with the results of ab-initio calculations presented recently by Balan et al. (2018). The results suggest that the mechanisms operating during carbonate mineral formation from an amorphous precursor are likely leading to near isotope equilibrium conditions between B in the solid and aqueous B species.

### **Acknowledgements**

This work was financially supported by the French National Programme SYSTER/INSU, the IPGP multidisciplinary program PARI, by Paris-IdF region SESAME Grant no. SESAME 12015908 and by the Austrian Science Fund (FWF) project number T 920-N29. Anna Harrison is highly acknowledged for her help with English. Finally, we wish to thank the Associate Editor Al Mucci, Jesse Farmer, Joji Uchikawa and Oscar Branson for their insightful and constructive comments on previous versions of this manuscript.

### **References**

- AlKhatib M. R. and Eisenhauer A. (2017) Calcium and strontium isotope fractionation in aqueous solutions as a function of temperature and reaction rate; II. Aragonite. *Geochim. Cosmochim. Acta* 209, 320–342.
- Allen, K.A., Honisch, B., Eggins, S.M., Yu, J.M., Spero, H.J. and Elderfield, H. (2011) Controls on boron incorporation in cultured tests of the planktic foraminifer *Orbulina universa*. *Earth Planet. Sci. Lett.* 309, 291-301.
- Allison J.D., Brown D.S. and Novo-Gradac K.J. (1991) MINTEQA2/PRODEFA2, A geochemical assessment model for environmental systems: Version 3.0 User's Manual. U.S. Environmental Protection Agency, Athens, GA.

- Baes C. F. and Mesmer R. S. (1976) *The Hydrolysis of Cations*. John Wiley and Sons, New York, London, Sydney, Toronto.
- Balan, E., Pietrucci, F., Gervais, C., Blanchard, M., Schott, J., Gaillardet, J. (2016) First-principles study of boron speciation in calcite and aragonite. *Geochim. Cosmochim. Acta* 193, 119-131.
- Balan, E., Noireaux, J., Mavromatis, V., Saldi, G.D., Montouillout, V., Blanchard, M., Pietrucci, F., Gervais, C., Rustad, J.R., Schott, J. and Gaillardet, J. (2018) Theoretical isotopic fractionation between structural boron in carbonates and aqueous boric acid and borate ion. *Geochim. Cosmochim. Acta* 222, 117-129.
- Branson, O., Kaczmarek, K., Redfern, S.A.T., Misra, S., Langer, G., Tylliszczak, T., Bijma, J. and Elderfield, H. (2015) The coordination and distribution of B in foraminiferal calcite. *Earth Planet. Sci. Lett.* 416, 67-72.
- Bushuev, Y.G., Finney, A.R. and Rodger, P.M. (2015) Stability and Structure of Hydrated Amorphous Calcium Carbonate. *Cryst. Growth Des.* 15, 5269-5279.
- Catanzaro E.J., Champion C.E., Garner E.L., Malinenko G., Sappenfeld K.M., Shields W.R. (1970) Boric acid, isotopic, and assay standard reference materials. US National Bureau of Standards Special Publication, 260, 17-70.
- DePaolo D.J. (2011) Surface kinetic model for isotopic and trace element fractionation during precipitation of calcite from aqueous solution. *Geochim. Cosmochim. Acta* 75, 1039-1056
- Dietzel, M., Purgstaller, B., Kluge, T., Leis, A. and Mavromatis, V. (2020) Oxygen and clumped isotope fractionation during the formation of Mg calcite via an amorphous precursor. *Geochim. Cosmochim. Acta*, 276, 258-273.
- Douville, E., Paterne, M., Cabioch, G., Louvat, P., Gaillardet, J., Juillet-Leclerc, A., Ayliffe, L., 2010. Abrupt sea surface pH change at the end of the Younger Dryas in the central

- sub-equatorial Pacific inferred from boron isotope abundance in corals (Porites). *Biogeosciences* 7, 2445–2459.
- Farmer, J.R., Branson, O., Uchikawa, J., Penman, D.E., Honisch, B. and Zeebe, R.E. (2019) Boric acid and borate incorporation in inorganic calcite inferred from B/Ca, boron isotopes and surface kinetic modeling. *Geochim. Cosmochim. Acta* 244, 229-247.
- Foster, G.L., 2008. Seawater pH, pCO<sub>2</sub> and [CO<sub>3</sub><sup>2-</sup>] variations in the Caribbean Sea over the last 130 kyr: a boron isotope and B/Ca study of planktic foraminifera. *Earth Planet. Sci. Lett.* 271, 254–266.
- Gautier, Q., Benzeth, P., Mavromatis, V., Schott, J., 2014. Hydromagnesite solubility product and growth kinetics in aqueous solution from 25 to 75°C. *Geochim. Cosmochim. Acta* 138, 1–20.
- Giuffre, A.J., Gagnon, A.C., De Yoreo, J.J. and Dove, P.M. (2015) Isotopic tracer evidence for the amorphous calcium carbonate to calcite transformation by dissolution–reprecipitation. *Geochim. Cosmochim. Acta* 165, 407-417.
- Goetschl K.E., Dietzel M., Purgstaller B., Grengg C. and Mavromatis V. (2021) Control of MgSO<sub>4</sub><sup>0</sup>(aq) on the transformation of amorphous calcium carbonate to high-Mg calcite and long-term reactivity of the crystalline solid. *Geochim. Cosmochim. Acta* (in press). DOI: 10.1016/j.gca.2021.07.026
- Gong, Y.U.T., Killian, C.E., Olson, I.C., Appathurai, N.P., Amasino, A.L., Martin, M.C., Holt, L.J., Wilt, F.H. and Gilbert, P. (2012) Phase transitions in biogenic amorphous calcium carbonate. *Proceedings of the National Academy of Sciences of the United States of America* 109, 6088-6093.
- Harrison A. L., Mavromatis V., Oelkers E. H. and Benzeth P. (2019) Solubility of the hydrated Mg-carbonates nesquehonite and dypingite from 5 to 35°C: Implications for CO<sub>2</sub> storage and the relative stability of Mg-carbonates. *Chem. Geol.* 504, 123–135.

- Hemming, N.G. and Hanson, G.N. (1992) Boron Isotopic Composition and Concentration in Modern Marine Carbonates. *Geochim. Cosmochim. Acta* 56, 537-543.
- Hemming, N.G., Reeder, R.J. and Hanson, G.N. (1995) Mineral-fluid partitioning and isotopic fractionation of boron in synthetic calcium carbonate. *Geochim. Cosmochim. Acta* 59, 371-379.
- Henehan, M.J., Rae, J.W.B., Foster, G.L., Erez, J., Prentice, K.C., Kucera, M., Bostock, H.C., Martínez-Botí, M.A., Milton, J.A., Wilson, P.A., Marshall, B.J., Elliott, T. (2013) Calibration of the boron isotope proxy in the planktonic foraminifera *Globigerinoides ruber* for use in palaeo-CO<sub>2</sub> reconstruction. *Earth Planet. Sci. Lett.* 364, 111–122.
- Hönisch, B., Bijma, J., Russell, A.D., Spero, H.J., Palmer, M.R., Zeebe, R.E., Eisenhauer, A. (2003) The influence of symbiont photosynthesis on the boron isotopic composition of foraminifera shells. *Mar. Micropaleontol.* 49, 87–96.
- Hönisch, B., Hemming, N.G., 2005. Surface ocean pH response to variations in pCO<sub>2</sub> through two full glacial cycles. *Earth Planet. Sci. Lett.* 236, 305–314.
- Ihli, J., Wong, W.C., Noel, E.H., Kim, Y.Y., Kulak, A.N., Christenson, H.K., Duer, M.J. and Meldrum, F.C. (2014) Dehydration and crystallization of amorphous calcium carbonate in solution and in air. *Nat. Commun.* 5.
- Jacob, D.E., Wirth, R., Agbaje, O.B.A., Branson, O., Eggins, S.M. (2017) Planktic foraminifera form their shells via metastable carbonate phases. *Nat. Commun.* 8.
- Jacob, D.E., Wirth, R., Soldati, A.L., Wehrmeister, U., Schreiber, A. (2011) Amorphous calcium carbonate in the shells of adult Unionoida. *J. Struct. Biol.* 173, 241-249.
- Kaczmarek, K., Nehrke, G., Misra, S., Bijma, J. and Elderfield, H. (2016) Investigating the effects of growth rate and temperature on the B/Ca ratio and  $\delta^{11}\text{B}$  during inorganic calcite formation. *Chem. Geol.* 421, 81-92.

- Klochko, K., Cody, G.D., Tossell, J.A., Dera, P. and Kaufman, A.J. (2009) Re-evaluating boron speciation in biogenic calcite and aragonite using B-11 MAS NMR. *Geochim. Cosmochim. Acta* 73, 1890-1900.
- Konrad, F., Purgstaller, B., Gallien, F., Mavromatis, V., Gane, P. and Dietzel, M. (2018) Influence of aqueous Mg concentration on the transformation of amorphous calcium carbonate. *J. Cryst. Growth* 498, 381-390.
- Lam, R.S.K., Charnock, J.M., Lennie, A. and Meldrum, F.C. (2007) Synthesis-dependant structural variations in amorphous calcium carbonate. *Crystengcomm* 9, 1226-1236.
- Loste, E., Wilson, R.M., Seshadri, R. and Meldrum, F.C. (2003) The role of magnesium in stabilising amorphous calcium carbonate and controlling calcite morphologies. *J. Cryst. Growth* 254, 206-218.
- Louvat, P., Bouchez, J. and Paris, G. (2011) MC-ICP-MS Isotope Measurements with Direct Injection Nebulisation (d-DIHEN): Optimisation and Application to Boron in Seawater and Carbonate Samples. *Geost. Geoanal. Res.*, 35: 75-88.
- Louvat P., Moureau J., Paris G., Bouchez J., Noireaux J., Gaillardet J. (2014) A fully automated direct injection nebulizer (d-DIHEN) for MC-ICP-MS isotope analysis: application to boron isotope ratio measurements. *J. Anal. Atom. Spectrom.*, 29, 1698-1707.
- Louvat P., Tharaud M., Buisson M., Rollion-Bard C., Benedetti M. F. (2019)  $\mu$ -dDIHEN: a new micro-flow liquid sample introduction system for direct injection nebulization in ICP-MS. *J. Anal. Atom. Spectrom.*, 34, 1553 – 1563.
- Martell, A.E., Smith, R., Motekaitis, R.J. (2004) NIST critically selected stability constants of metal complexes. NIST Stand. Ref. Database46.
- Mass, T., Giuffre, A.J., Sun, C.Y., Stifler, C.A., Frazier, M.J., Neder, M., Tamura, N., Stan, C.V., Marcus, M.A., Gilbert, P. (2017) Amorphous calcium carbonate particles form coral skeletons. *Proceedings of the National Academy of Sciences of the United States of America* 114, E7670-E7678.

- Massiot, D., Fayon, F., Capron, M., King, I., Le Calvé, S., Alonso, B., Durand, J.-O., Bujoli, B., Gan, Z. and Hoatson, G. (2002) Modelling one- and two-dimensional solid-state NMR spectra," *Magn. Reson. Chem.*, 40, 70-76.
- Mavromatis, V., Harrison, A.L., Eisenhauer, A. and Dietzel, M. (2017a) Strontium isotope fractionation during strontianite ( $\text{SrCO}_3$ ) dissolution, precipitation and at equilibrium. *Geochim. Cosmochim. Acta* 218, 201-214.
- Mavromatis, V., Montouillout, V., Noireaux, J., Gaillardet, J. and Schott, J. (2015) Characterization of boron incorporation and speciation in calcite and aragonite from co-precipitation experiments under controlled pH, temperature and precipitation rate. *Geochim. Cosmochim. Acta* 150, 299-313.
- Mavromatis, V., Purgstaller, B., Dietzel, M., Buhl, D., Immenhauser, A. and Schott, J. (2017b) Impact of amorphous precursor phases on magnesium isotope signatures of Mg-calcite. *Earth Planet. Sci. Lett.* 464, 227-236.
- Mavromatis, V., Schmidt, M., Botz, R., Comas-Bru, L. and Oelkers, E.H. (2012) Experimental quantification of the effect of Mg on calcite-aqueous fluid oxygen isotope fractionation. *Chem. Geol.* 310-311, 97-105.
- Mavromatis, V., van Zuilen, K., Purgstaller, B., Baldermann, A., Nögler, T.F. and Dietzel, M. (2016) Barium isotope fractionation during witherite ( $\text{BaCO}_3$ ) dissolution, precipitation and at equilibrium. *Geochim. Cosmochim. Acta* 190, 72-84.
- Mavromatis V., van Zuilen K., Blanchard M., van Zuilen M., Dietzel M. and Schott J. (2020) Experimental and theoretical modelling of kinetic and equilibrium Ba isotope fractionation during calcite and aragonite precipitation. *Geochim. Cosmochim. Acta* 269, 566–580.
- McElligott S. and Byrne R.H. (1998) Interaction of  $\text{B}(\text{OH})_3$  and  $\text{HCO}_3^-$  in seawater: Formation of  $\text{B}(\text{OH})_2\text{CO}_3^-$ . *Aquatic Geochem.* 3, 345-356.

- Nielsen, M.H., Aloni, S. and De Yoreo, J.J. (2014) In situ TEM imaging of CaCO<sub>3</sub> nucleation reveals coexistence of direct and indirect pathways. *Science* 345, 1158-1162.
- Nir, O., Vengosh, A., Harkness, J.S., Dwyer, G.S. and Lahav, O. (2015) Direct measurement of the boron isotope fractionation factor: Reducing the uncertainty in reconstructing ocean paleo-pH. *Earth Planet. Sci. Lett.* 414, 1-5.
- Noireaux J., Mavromatis V., Gaillardet J., Schott J., Montouillout V., Louvat P., Rollion-Bard C. and Neuville D. R. (2015) Crystallographic control on the boron isotope paleo-pH proxy. *Earth Planet. Sci. Lett.* 430, 398-407.
- Oelkers, E.H., von Strandmann, P. and Mavromatis, V. (2019) The rapid resetting of the Ca isotopic signatures of calcite at ambient temperature during its congruent dissolution, precipitation, and at equilibrium. *Chem. Geol.* 512, 1-10.
- Ogino, T., Suzuki, T. and Sawada, K. (1987) The formation and transformation mechanism of calcium carbonate in water. *Geochim. Cosmochim. Acta* 51, 2757-2767.
- Paris, G., Bartolini, A., Donnadiou, Y., Beaumont, V., Gaillardet, J., 2010. Investigating boron isotopes in a middle Jurassic micritic sequence: primary vs. diagenetic signal. *Chem. Geol.* 275, 117–126.
- Parkhurst, D.L. and Appelo, C.A.J. (2013). Description of input and examples for PHREEQC version 3: a computer program for speciation, batch-reaction, one-dimensional transport, and inverse geochemical calculations (USGS Numbered Series No. 6-A43). In: *Techniques and Methods*, U.S. Geological Survey. Reston, VA.
- Pearce, C.R., Saldi, G.D., Schott, J. and Oelkers, E.H. (2012) Isotopic fractionation during congruent dissolution, precipitation and at equilibrium: Evidence from Mg isotopes. *Geochim. Cosmochim. Acta* 92, 170-183.
- Pokrovski, G.S., Schott, J. and Sergeev, A.S. (1995) Experimental-Determination of the Stability-Constants of NaSO<sub>4</sub><sup>-</sup> and NaB(OH)<sub>4</sub><sup>0</sup> in Hydrothermal Solutions Using a New

- High-Temperature Sodium-Selective Glass-Electrode - Implications for Boron Isotopic Fractionation. *Chem. Geol.* 124, 253-265.
- Politi, Y., Arad, T., Klein, E., Weiner, S. and Addadi, L. (2004) Sea urchin spine calcite forms via a transient amorphous calcium carbonate phase. *Science* 306, 1161-1164.
- Politi, Y., Metzler, R.A., Abrecht, M., Gilbert, B., Wilt, F.H., Sagi, I., Addadi, L., Weiner, S. and Gilbert, P. (2008) Transformation mechanism of amorphous calcium carbonate into calcite in the sea urchin larval spicule. *Proceedings of the National Academy of Sciences of the United States of America* 105, 17362-17366.
- Purgstaller, B., Dietzel, M., Baldermann, A. and Mavromatis, V. (2017a) Control of temperature and aqueous  $Mg^{2+}/Ca^{2+}$  ratio on the (trans-) formation of ikaite. *Geochim. Cosmochim. Acta* 217, 128-143.
- Purgstaller, B., Goetschl, K. E., Mavromatis, V., Dietzel, M. (2019) Solubility Investigations in the Amorphous Calcium Magnesium Carbonate System. *CrystEngComm*, 21, 155–164.
- Purgstaller, B., Konrad, F., Dietzel, M., Immenhauser, A. and Mavromatis, V. (2017b) Control of  $Mg^{2+}/Ca^{2+}$  Activity Ratio on the Formation of Crystalline Carbonate Minerals via an Amorphous Precursor. *Cryst. Growth Des.* 17, 1069-1078.
- Purgstaller, B., Mavromatis, V., Immenhauser, A. and Dietzel, M. (2016) Transformation of Mg-bearing amorphous calcium carbonate to Mg-calcite – In situ monitoring. *Geochim. Cosmochim. Acta* 174, 180-195.
- Rae, J.W.B., Foster, G.L., Schmidt, D.N., Elliott, T. (2011). Boron isotopes and B/Ca in benthic foraminifera: proxies for the deep ocean carbonate system. *Earth Planet. Sci. Lett.* 302, 403–413.
- Radha, A.V. and Navrotsky, A. (2015) Direct Experimental Measurement of Water Interaction Energetics in Amorphous Carbonates  $MCO_3$  (M = Ca, Mn, and Mg) and Implications for Carbonate Crystal Growth. *Cryst. Growth Des.* 15, 70-78.

- Rodriguez-Navarro, C., Kudlacz, K., Cizer, O. and Ruiz-Agudo, E. (2015) Formation of amorphous calcium carbonate and its transformation into mesostructured calcite. *Crystengcomm* 17, 58-72.
- Rollion-Bard, C. and Erez, J., (2010) Intra-shell boron isotope ratios in the symbiont-bearing benthic foraminiferan *Amphistegina lobifera*: implications for  $\delta^{11}\text{B}$  vital effects and paleo-pH reconstructions. *Geochim. Cosmochim. Acta* 74, 1530–1536.
- Rollion-Bard, C., Blamart, D., Trebosc, J., Tricot, G., Mussi, A. and Cuif, J.P. (2011) Boron isotopes as pH proxy: A new look at boron speciation in deep-sea corals using B-11 MAS NMR and EELS. *Geochim. Cosmochim. Acta* 75, 1003-1012.
- Saldi, G.D., Noireaux, J., Louvat, P., Faure, L., Balan, E., Schott, J. and Gaillardet, J. (2018) Boron isotopic fractionation during adsorption by calcite – Implication for the seawater pH proxy. *Geochim. Cosmochim. Acta* 240, 255-273.
- Sen, S., Stebbins, J.F., Hemming, N.G. and Ghosh, B. (1994) Coordination Environments of B-Impurities in Calcite and Aragonite Polymorphs - a  $^{11}\text{B}$  MAS NMR Study. *Am. Miner.* 79, 819-825.
- Trotter, J., Montagna, P., McCulloch, M., Silenzi, S., Reynaud, S., Mortimer, G., Martin, S., Ferrier-Pagès, C., Gattuso, J.-P. and Rodolfo-Metalpa, R. (2011) Quantifying the pH ‘vital effect’ in the temperate zooxanthellate coral *Cladocora caespitosa*: Validation of the boron seawater pH proxy. *Earth Planet. Sci. Lett.* 303, 163-173.
- Uchikawa, J., Harper, D.T., Penman, D.E., Zachos, J.C. and Zeebe, R.E. (2017) Influence of solution chemistry on the boron content in inorganic calcite grown in artificial seawater. *Geochim. Cosmochim. Acta* 218, 291-307.
- Uchikawa, J., Penman, D.E., Zachos, J.C. and Zeebe, R.E. (2015) Experimental evidence for kinetic effects on B/Ca in synthetic calcite: Implications for potential  $\text{B}(\text{OH})_4^-$  and  $\text{B}(\text{OH})_3$  incorporation. *Geochim. Cosmochim. Acta* 150, 171-191.

Vogl J., Rosner M. (2011) Production and Certification of a Unique Set of Isotope and Delta Reference Materials for Boron Isotope Determination in Geochemical, Environmental and Industrial Materials. *Geost. Geoanal. Res.*, 36, 161-175.

Table 1: Chemical composition of reactive fluids and solids, saturation index with respect to calcite and aragonite in the aqueous phase and mineralogy of the precipitated phase together with distribution coefficients and growth rate estimates. Mhc, Ar, Hmg and Cc, denote monohydrocalcite, aragonite, hydromagnesite and calcite respectively.

Experiment	Time (min)	pH	Fluids							Solids		LogD <sub>B</sub>	Rate (mmol/s)	Rate (mol/m <sup>2</sup> /s)	Mineralogy*	
			Ca (mM)	Mg (mM)	B (mM)	Alkalinity (mM)	Ionic Strength (mM)	SI <sub>calcite</sub>	SI <sub>aragonite</sub>	Mg (mg/kg)	B (mg/kg)					
B1	0	8.80	0.1		16.5	1160.2	859.6	1.1	0.9							
	1	8.81	2.8	3.7	15.4	1076.7	842.1	2.5	2.3				2.67E-01	3.33E-06		Mg-ACC
	5	8.82	0.5	15.1	12.9	795.2	776.8	1.8	1.6	17355	416	-2.13	2.53E-01	6.67E-07		Mg-ACC
	9	8.81	2.1	20.7	10.3	585.9	719.7	2.3	2.1				2.16E-01	3.70E-07		Mg-ACC
	12.5	8.80	2.5	23.6	9.0	449.6	681.3	2.4	2.2				1.92E-01	2.67E-07		Mg-ACC
	18	8.83	3.2	26.4	7.1	297.0	637.6	2.4	2.3				1.63E-01	1.85E-07		Mg-ACC
	25	8.85	3.4	27.8	5.6	153.4	605.0	2.3	2.2	24438	602	-2.05	1.40E-01	1.33E-07		Mg-ACC
	30	8.82	3.4	28.1	5.3	140.3	596.9	2.3	2.1	26381	424	-2.25	1.16E-01	1.11E-07		Mg-ACC
	40	8.82	3.4	29.2	5.7	138.4	595.5	2.3	2.1	25739	509	-2.35	8.69E-02	8.33E-08		Mg-ACC
	50	8.82	3.3	28.6	5.5	139.6	596.8	2.3	2.1				6.98E-02	6.67E-08		Mg-ACC
	60	8.82	3.1	27.9	5.5	134.6	593.4	2.3	2.1	25445	477	-2.45	5.84E-02	5.56E-08		Mg-ACC
	100	9.02	0.5	40.2	5.9	169.1	611.8	1.6	1.4	13327	368	-2.53	3.34E-02	3.33E-08		mhc
	180	9.05	0.3	45.3	6.3	179.2	616.9	1.3	1.2	11349	342	-2.58	1.81E-02	1.85E-08		mhc
	1440	8.95	0.2	34.2	6.3	161.1	608.4	1.2	1.0	17438	320	-2.45	2.39E-03	2.31E-09		mhc (99) + hmg (1)
	4320	8.90	0.2	26.9	6.4	146.5	599.4	1.1	0.9	26753	237	-2.58	8.26E-04	7.72E-10		mhc (98) + hmg (2)
	20160	9.08	0.2	17.7	5.9	141.1	592.2	1.2	1.0	31443	274	-2.59	1.85E-04	1.65E-10		mhc (96) + hmg (4)
66240	8.86	0.1	12.9	6.3	115.6	577.5	0.0	-0.2	32694	121	-3.01	5.74E-05	5.03E-11		Ar (95) + Hmg (4) + Cc (1)	
786240	8.87	0.1	10.0	6.4	132.2	588.9	0.0	-0.1	34225	242	-2.58	4.90E-06	4.24E-12		Ar (94) + Hmg (5) + Cc (1)	
934560	8.80	0.1	9.7	7.9	125.7	585.3	0.0	-0.2	36724	184	-2.91	4.13E-06	3.57E-12		Ar (94) + Hmg (5) + Cc (1)	
1071360	9.38	0.1	9.3	6.3	135.7	585.2	0.2	0.0	38969	166	-2.90	3.61E-06	3.11E-12		Ar (90) + Hmg (9) + Cc (1)	
B2	0	8.37	0.1		17.1	1082.2	841.0	0.9	0.7							
	1	8.32	2.8	4.2	15.9	1002.7	827.5	2.2	2.0				2.63E-01	3.33E-06		Mg-ACC
	5	8.30	2.1	16.5	13.0	722.1	755.0	2.1	1.9	14403	566	-2.34	2.45E-01	6.67E-07		Mg-ACC
	9	8.31	4.6	24.8	11.4	512.2	687.9	2.4	2.2				2.03E-01	3.70E-07		Mg-ACC
	12.5	8.34	4.0	25.6	9.1	408.8	667.4	2.3	2.1	19764	593	-2.40	1.86E-01	2.67E-07		Mg-ACC
	18	8.35	4.6	26.9	7.0	242.2	610.6	2.3	2.1				1.60E-01	1.85E-07		Mg-ACC
	25	8.31	7.0	30.8	5.9	121.5	588.9	2.3	2.1	22796	439	-2.57	1.34E-01	1.33E-07		Mg-ACC
	30	8.36	6.3	29.6	5.7	125.4	588.9	2.3	2.1	26600	348	-2.76	1.12E-01	1.11E-07		Mg-ACC
	40	8.31	4.9	28.1	6.0	114.7	581.1	2.1	1.9	28069	354	-3.02	8.50E-02	8.33E-08		Mg-ACC, Mg-calcite
	50	8.32	0.6	15.3	6.2	98.3	558.1	1.2	1.0				7.30E-02	6.67E-08		Mg-calcite
	60	8.32	0.4	13.5	6.3	95.7	555.5	1.0	0.8	33923	225	-3.24	6.13E-02	5.56E-08		Mg-calcite
	100	8.31	0.2	11.2	6.3	90.0	549.5	0.6	0.4	36814	210	-3.31	3.72E-02	3.33E-08		Mg-calcite
	180	8.33	0.1	9.8	6.3	89.0	548.0	0.4	0.2	36232	268	-3.22	2.08E-02	1.85E-08		Mg-calcite
1440	8.27	0.1	6.4	6.3	82.0	541.3	0.4	0.2	37722	266	-3.25	2.64E-03	2.31E-09		Mg-calcite	

	4320	8.10	0.1	4.8	5.9	81.4	540.4	0.3	0.2	40123	254	-3.26	8.85E-04	7.72E-10	Mg-calcite
	20160	8.01	0.1	2.5	5.9	79.0	537.9	0.1	-0.1	40939	193	-3.46	1.92E-04	1.65E-10	Mg-calcite
	786240	8.18	0.1	0.5	5.6	72.7	531.5	0.2	0.0	42064	254	-3.46	-1.30E-08	4.24E-12	Mg-calcite
	934560	8.32	0.1	0.3	6.2	71.0	529.4	0.3	0.1	41133	185	-3.69	-6.91E-09	3.57E-12	Mg-calcite
	1071360	8.13	0.1	0.3	5.0	76.0	534.0	0.2	0.0	44894	159	-3.61	3.64E-06	3.11E-12	Mg-calcite
B3	0	8.80	0.1	0.06	16.3	1191.4	877.5	1.1	0.9						
	1	8.81	3.1	1.80	14.8	1100.3	857.1	2.5	2.3				3.00E-01	3.33E-06	Mg-ACC
	5	8.80	2.6	6.50	12.1	787.0	780.9	2.4	2.2	12444	465	-2.08	2.84E-01	6.67E-07	Mg-ACC
	9	8.81	2.2	8.74	9.3	563.6	715.6	2.3	2.2				2.43E-01	3.70E-07	Mg-ACC
	12.5	8.80	2.5	11.26	9.2	429.3	677.3	2.4	2.2	15396	364	-2.19	2.13E-01	2.67E-07	Mg-ACC
	18	8.86	2.4	11.45	6.8	254.3	614.5	2.3	2.1				1.80E-01	1.85E-07	Mg-ACC
			3.7	14.49	6.2	121.2	583.0	2.3	2.2	16963	323	-2.33	1.49E-01	1.33E-07	Mg-ACC, Mg-calcite
	25	8.84													
			2.9	13.06	5.6	105.8	560.7	2.2	2.1	17174	309	-2.39	1.23E-01	1.11E-07	Mg-ACC, Mg-calcite
	30	8.90													
	40	8.82	0.2	3.42	6.6	90.5	546.7	1.1	0.9	24930	207	-2.87	9.67E-02	8.33E-08	Mg-calcite
	50	8.83	0.1	2.09	6.4	90.2	545.2	0.8	0.6				7.78E-02	6.67E-08	Mg-calcite
	60	8.83	0.1	1.85	6.8	90.1	545.2	0.7	0.5	25924	198	-3.00	6.49E-02	5.56E-08	Mg-calcite
	100	8.83	0.1	1.33	6.6	90.7	545.9	0.5	0.3	25721	209	-2.96	3.90E-02	3.33E-08	Mg-calcite
	180	8.84	0.1	1.06	6.4	90.0	544.9	0.4	0.3	26403	189	-3.03	2.17E-02	1.85E-08	Mg-calcite
	1440	9.01	0.0	0.99	6.2	90.3	543.8	0.4	0.2	25043	167	-3.07	2.71E-03	2.31E-09	Mg-calcite
	4320	9.15	0.1	0.54	6.2	87.5	540.5	0.6	0.4	26149	183	-3.01	9.06E-04	7.72E-10	Mg-calcite
	20160	8.86	0.04	0.28	6.1	89.0	543.9	0.4	0.2	26165	177	-2.91	1.94E-04	1.65E-10	Mg-calcite
	786240	9.26	0.04	0.05	6.4	96.5	547.5	0.5	0.3	23926	238	-2.73	4.99E-06	4.24E-12	Mg-calcite
	934560	9.35	0.04	0.05	6.5	95.2	545.5	0.5	0.3	27587	211	-2.92	4.20E-06	3.57E-12	Mg-calcite
	1071360	9.36	0.02	0.06	5.7	97.4	547.2	0.5	0.4	26809	151	-2.84	3.66E-06	3.11E-12	Mg-calcite

\*numbers in parentheses denote wt % of the mineral in the solid phase.

Table 2: Boron isotope composition of reactive fluids and solids, boron isotope fractionation factors and percentage of  $\text{BOH}_4^-$  species in the solid phase identified by  $^{11}\text{B}$  NMR spectroscopy and in the fluid phase defined using speciation calculations. Note that the decrease in the  $\Delta^{11}\text{B}_{\text{solid-B4}}$  value observed in experiment B1 is likely an artefact of  $\Delta^{11}\text{B}_{\text{solid-B4}}$  estimation due to pH increase by 0.6 units at the last measurement of this experiment (see Table 1).

Experiment	Time (min)	$\delta^{11}\text{B}_{\text{fluid}}$	2.s.d.	$\delta^{11}\text{B}_{\text{solid}}$	2 s.d.	$\Delta^{11}\text{B}_{\text{solid-fluid}}$	$\Delta^{11}\text{B}_{\text{solid-B4}}$	NMR $\text{BO}_4$ (%)	Aq. $\text{BOH}_4^-$ (%)	Aq. $\text{BOH}_4^-$ (%)*
B1	5	0.1	0.96	-6.77	0.54	-6.87	0.81	38	25	38
	25	3.95	0.37	-9.51	0.25	-13.46	-2.98	46	33	51
	100	0.96	0.37	-6.3	0.25	-7.26	1.1		39	62
	4320	-0.09	0.33	-3.82	0.25	-3.73	6.27	43	35	54
	66240	-0.66	0.25	-6.05	0.25	-5.39	5.45	36	35	51
	786240	-0.15	0.25	-4.04	0.44	-3.89	6.75	54	35	51
	934560	-0.53	0.25	-3.96	0.3	-3.43	8.08	63	33	47
	1071360	-0.01	0.25	-4.42	0.25	-4.41	0.72	37	55	78
B2	5	1.28	0.5	-8.5	0.25	-9.78	-0.4	37	9	14
	25	2.51	0.87	-13.35	0.84	-15.86	0.17	46	15	24
	100	0.16	0.41	-11.52	0.25	-11.68	5.27	34	15	22
	1440	1.05	0.32	-11.42	0.25	-12.47	5.05		14	20
	20160	1.26	0.25	-9.6	0.55	-10.86	8.3	37	9	12
	786240	0.46	0.25	-9.4	0.4	-9.86	8.55		12	17
	934560	0.21	0.25	-11.43	0.25	-11.64	5.82		16	22
	1071360	0.32	0.25	-12.66	0.32	-12.98	5.63	51	11	15
B3	5	0.03	0.6	-9.4	0.25	-9.43	-1.64		24	37
	25	2.66	0.25	-9.47	0.78	-12.13	-1.11	50	34	50
	40	0.71	0.25	-9.16	0.5	-9.87	1.97	46	35	48
	1440	0.44	0.25	-8.93	0.53	-9.37	0.17	54	43	59
	20160	0.56	0.68	-8.4	0.25	-8.96	2.46	57	36	50
	786240	0.09	0.25	-6.37	0.25	-6.46	0.14		53	72
	934560	0.03	0.25	-6.77	0.25	-6.8	-1.05		56	76
	1071360	1.33	0.25	-8.83	0.25	-10.16	-4.53	74	56	77
B stock		-0.29	0.25							

\*Denotes the sum of aqueous  $\text{B}(\text{OH})_4^-$  species including complexes with Na, Mg and Ca.

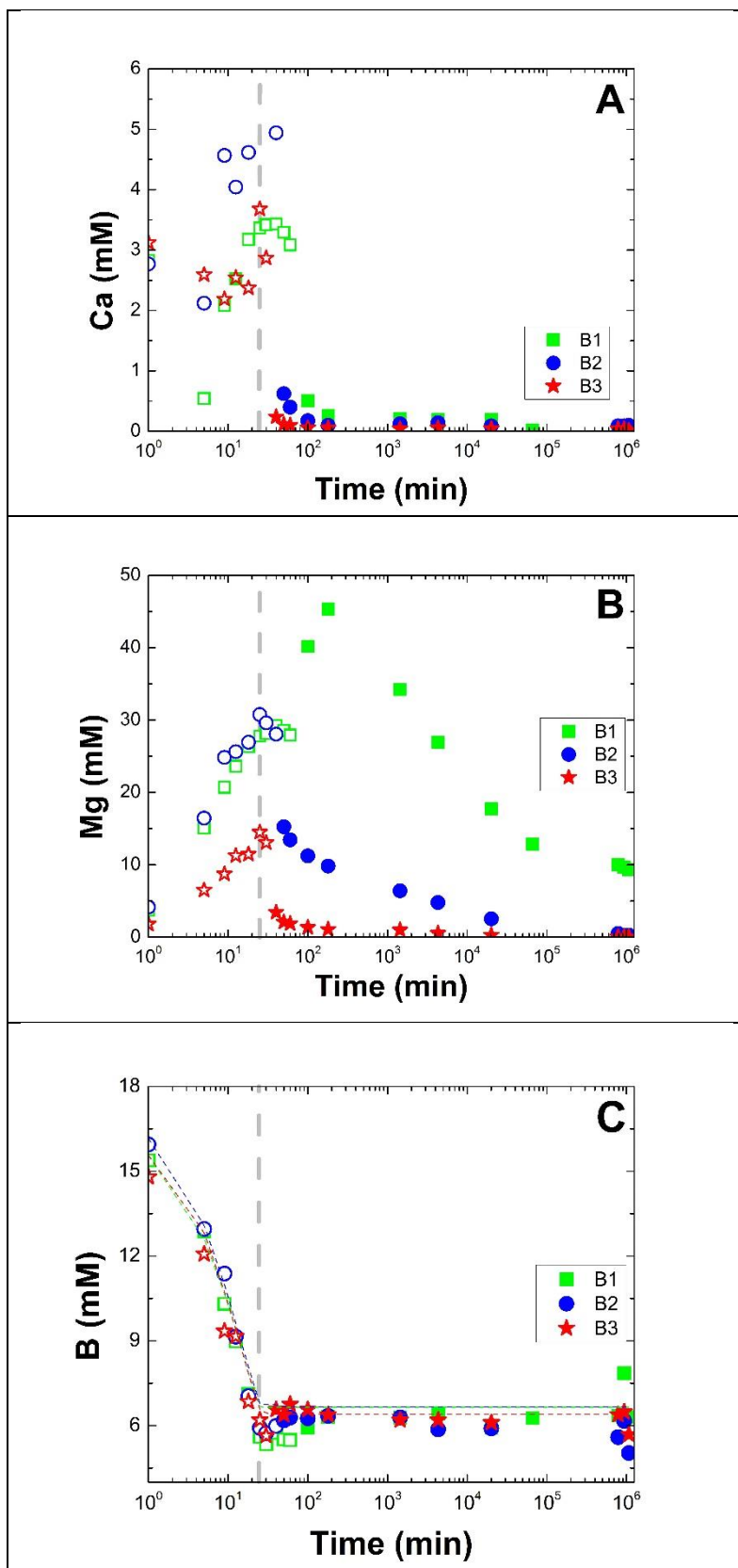


Figure 1: Temporal evolution of A) calcium concentration, B) magnesium concentration and C) boron concentration in the reactive fluids and theoretical B concentration due to dilution during the experimental runs (dashed lines). The grey vertical dashed line denotes the termination of the titration of the  $(\text{Ca,Mg})\text{Cl}_2$  inlet solution after 25 min of reaction time. The open symbols denote the presence of amorphous solids. Analytical uncertainties are included in the symbol size.

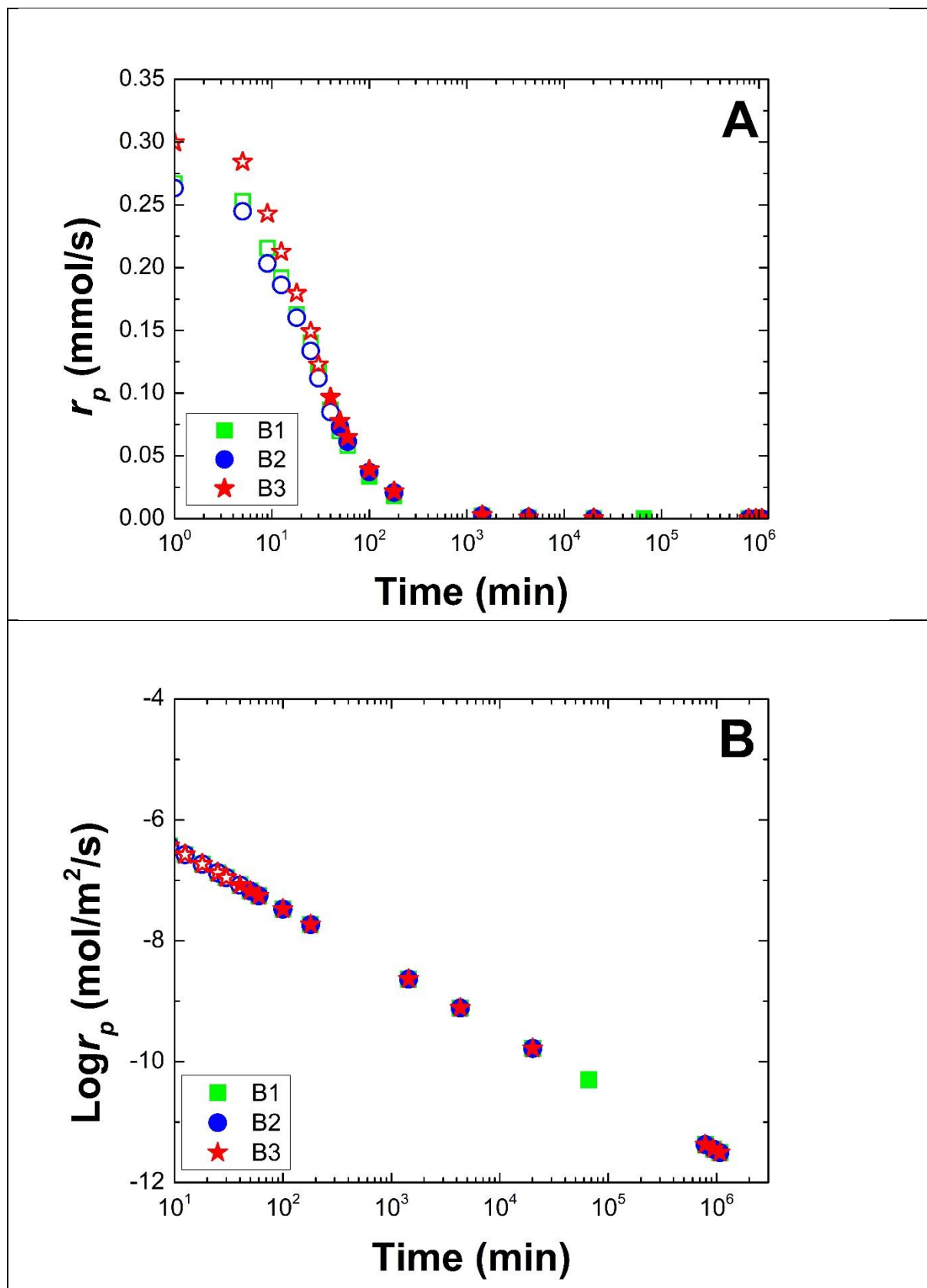


Figure 2: Temporal evolution of the growth rate ( $r_p$ ) calculated according to Eq. (1) (A) and estimated assuming a specific surface area of the precipitated solids of 50 m<sup>2</sup>/g (B). The open symbols denote the presence of amorphous solids.

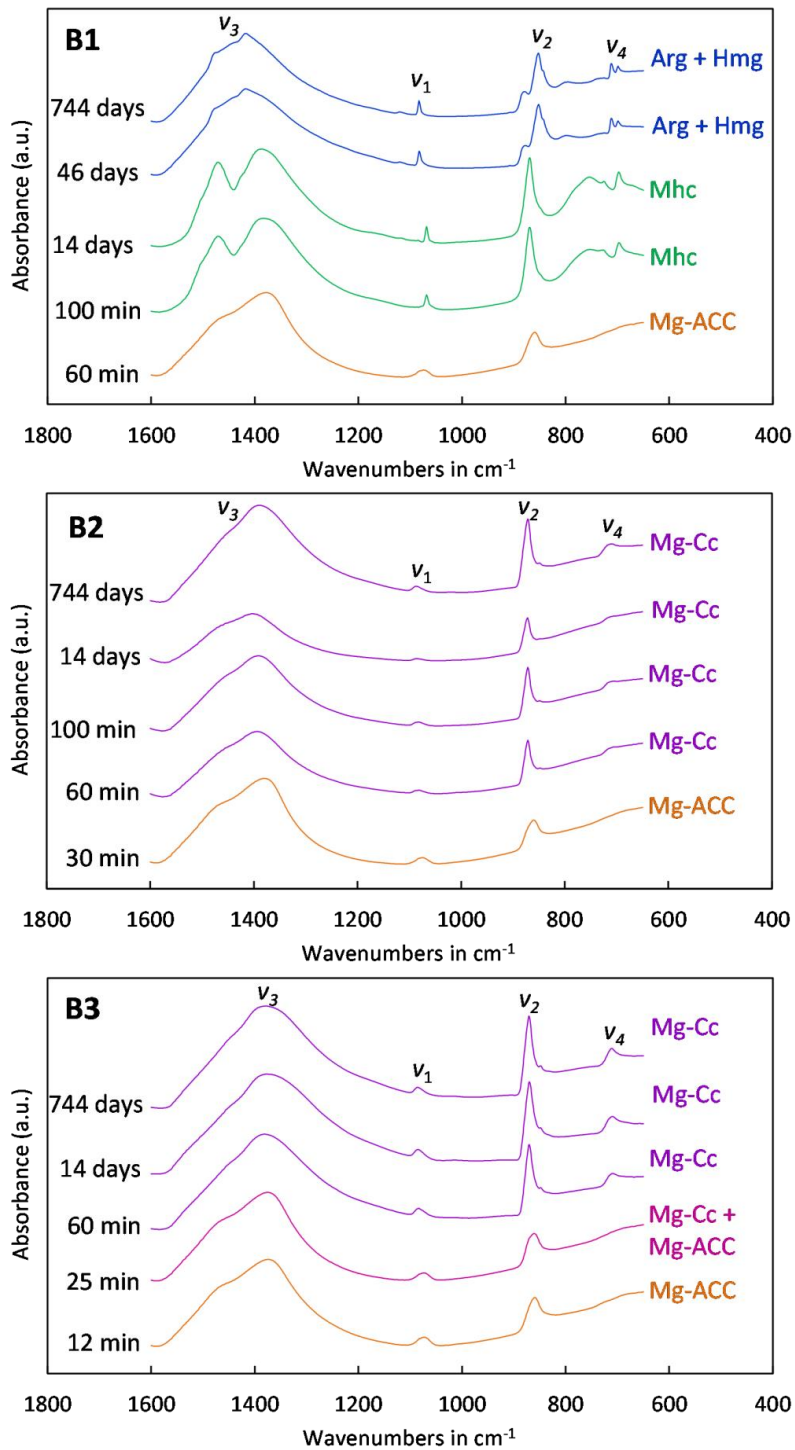


Figure 3. ATR-FTIR spectra of sampled precipitates at certain reaction times of the experiments B1, B2 and B3. Mg-Cc: Mg-rich calcite; Mhc: monohydrocalcite; Hmg: hydromagnesite; Arg: aragonite.

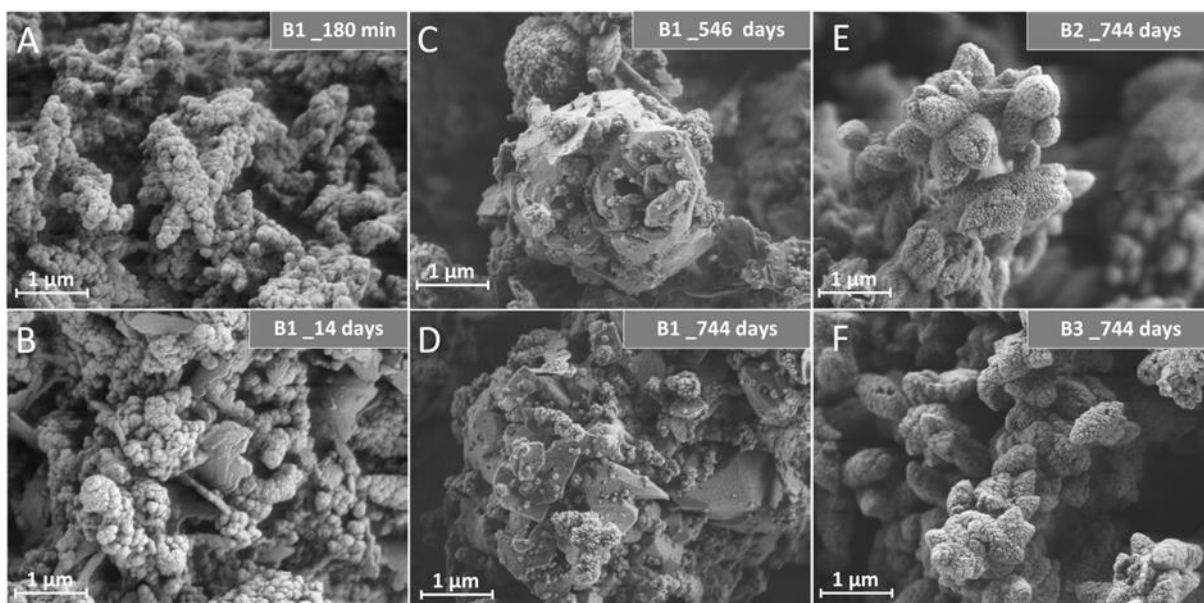


Figure 4. SEM images of sampled precipitates from experiment B1 after 180 min (A), 14 days (B), 546 days (C) and 744 days (D) of reaction time and from experiments B2 (E) and B3 (F) after 744 days of reaction time.

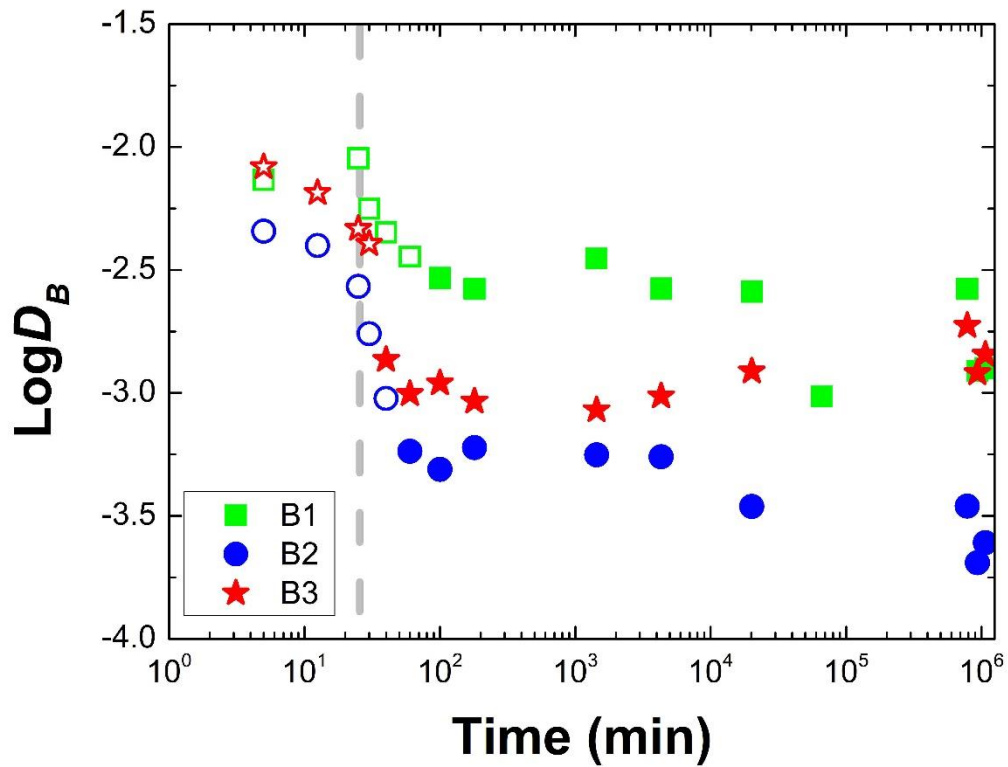


Figure 5: Temporal evolution of the boron partition coefficient (i.e.  $D_B = \frac{(X_B)_{CaCO_3}}{([B_T]/[CO_3^{2-}])_{fluid}}$ ) between the solid and fluid for experiments B1, B2 and B3. The grey vertical dashed line denotes the termination of the titration of the (Ca,Mg)Cl<sub>2</sub> inlet solution after 25 min of reaction time. The open symbols denote amorphous solids. Analytical uncertainties are included in the symbol size.

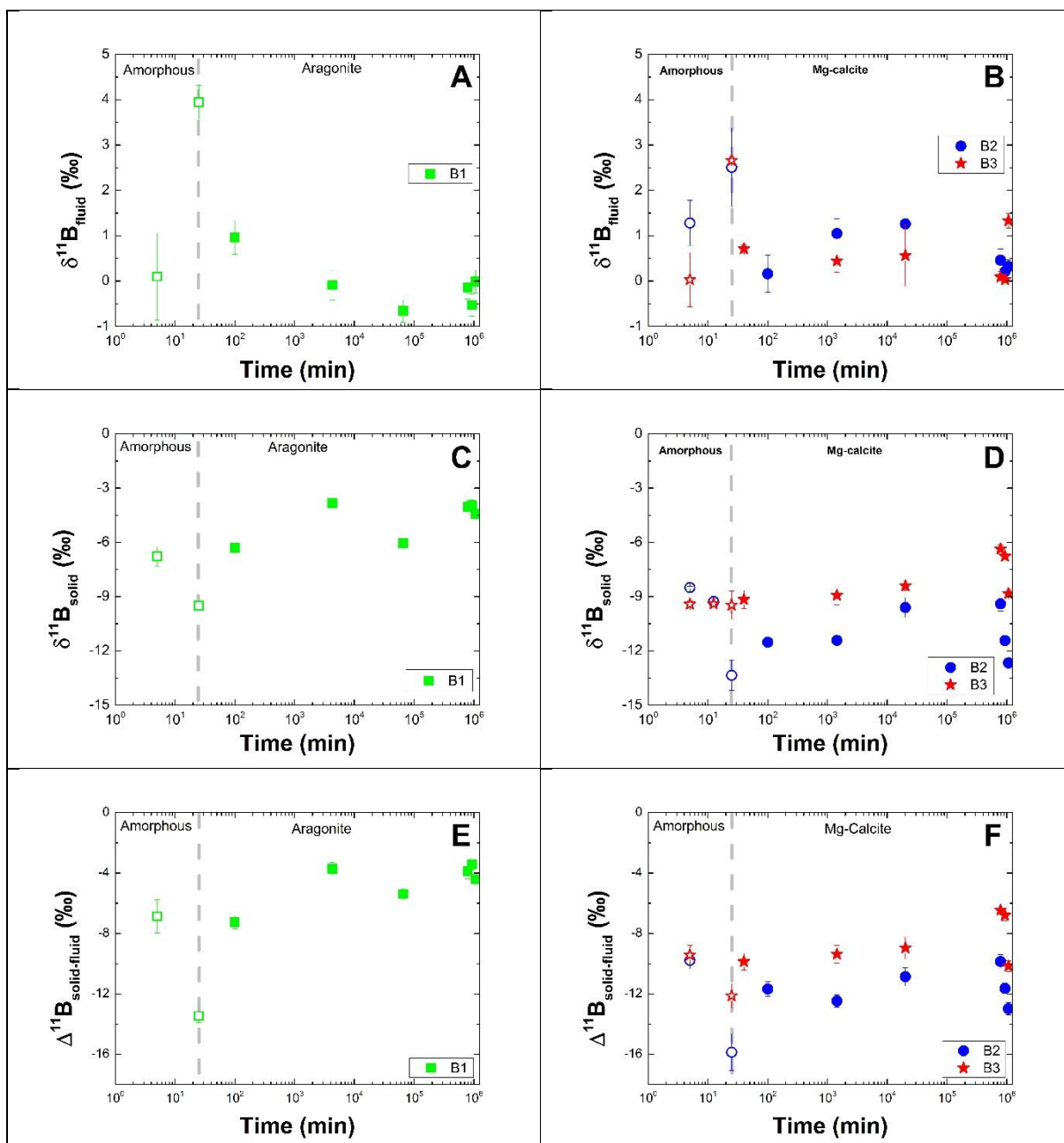


Figure 6: Temporal evolution of the  $\delta^{11}\text{B}$  value of reactive fluids (A-B), the  $\delta^{11}\text{B}$  value of bulk solids (C-D) and the isotope fractionation  $\Delta^{11}\text{B}_{\text{solid-fluid}}$  as it has been defined according to Eq. 2 (E-F). The grey vertical dashed line denotes the termination of the titration of the (Ca,Mg)Cl<sub>2</sub> inlet solution after 25 min of reaction time. The open symbols denote the presence of amorphous solids.

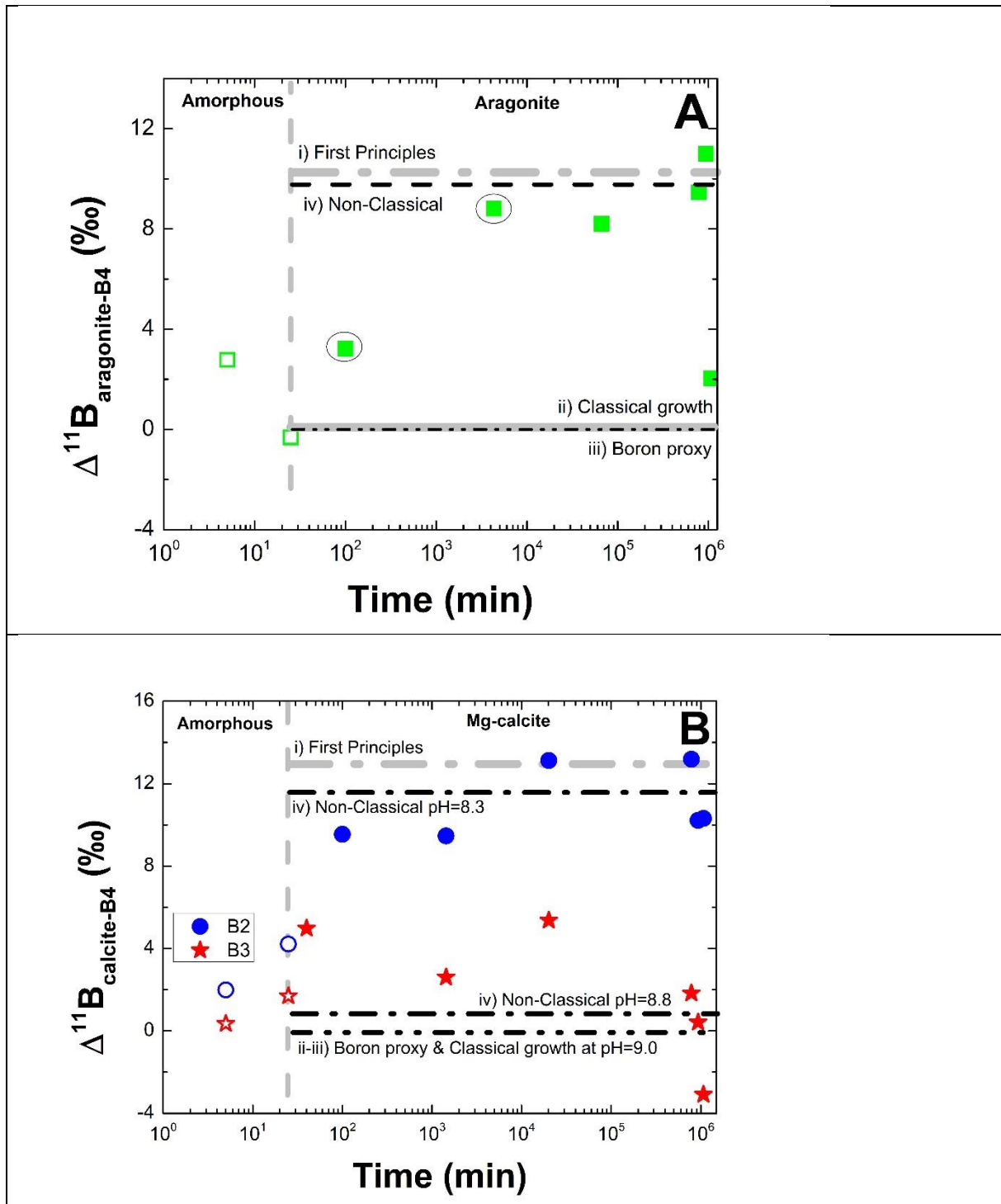


Figure 7: Temporal evolution of the boron isotope fractionation between A) aragonite and B) calcite and borate species in the reactive fluid estimated with the aid of Eq. (4) and  $\alpha_B=1.0326$ . The symbols in circles represent monohydrocalcite. The open symbols denote the presence of amorphous solids. The horizontal lines denote B isotope fractionation between the solid and aqueous borate as it is defined by i) first principle estimates, ii) classical growth experiments, iii) the boron pH-proxy that assume no fractionation between aqueous borate ion and the solid and iv) the average value of non-classical growth experiments of this study. The vertical grey dashed line denotes the termination of the titration of the (Ca,Mg)Cl<sub>2</sub> inlet solution after 25 min of reaction time. Analytical uncertainties are included in the symbol size.

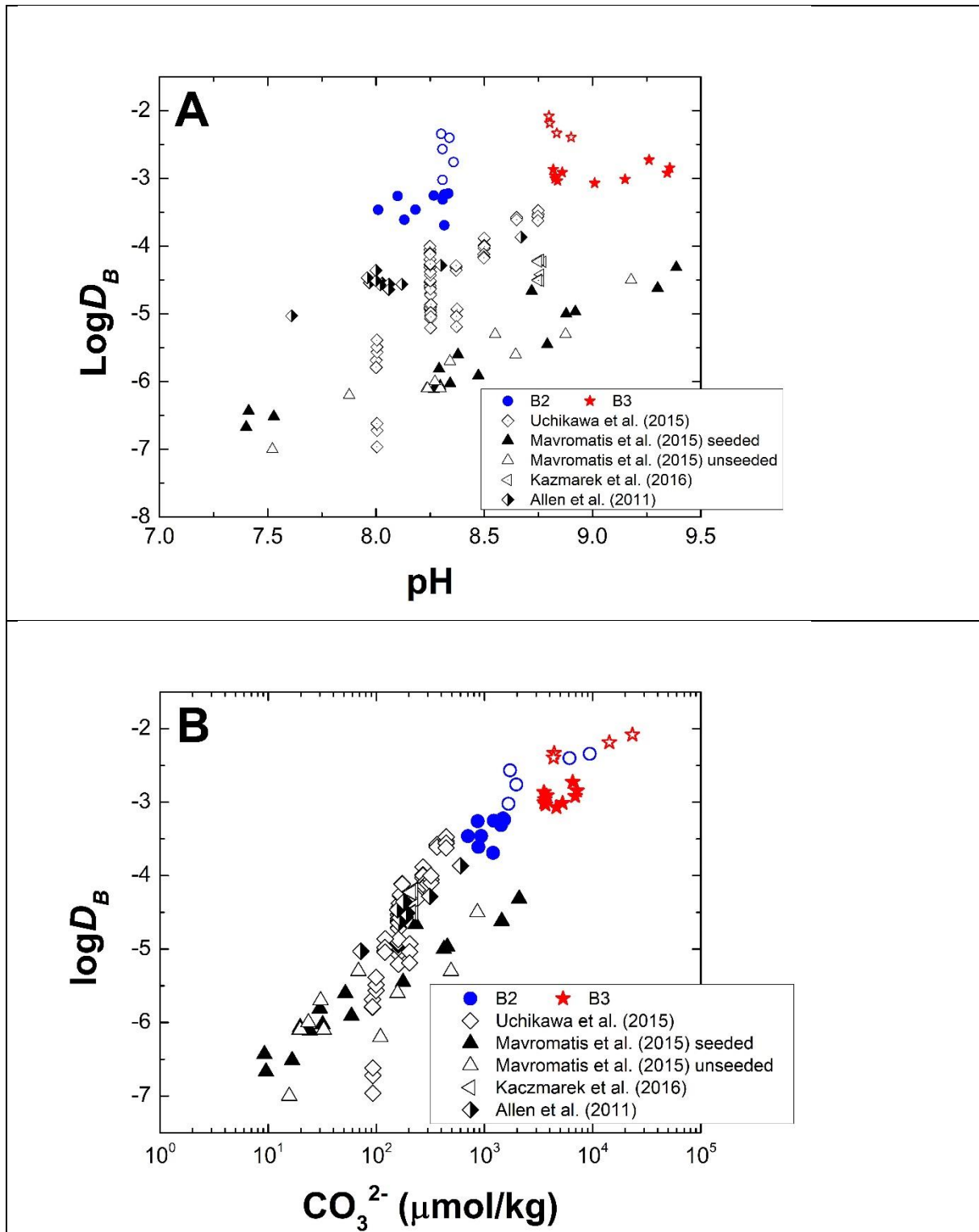


Figure 8: Boron distribution coefficient (i.e.  $D_B = \frac{(X_B)_{\text{CaCO}_3}}{([B_T]/[\text{CO}_3^{2-}])_{\text{fluid}}}$ ) as a function of pH (A) and aqueous  $\text{CO}_3^{2-}$  concentration (B) estimated using Eq. (2) for experiments B2 and B3 that yield Mg-calcite and recalculated values for inorganic calcite from the literature. The open coloured symbols denote amorphous solids. Allen et al. (2011) data correspond to culture experiments with planktonic foraminifer *Orbulina universa*.

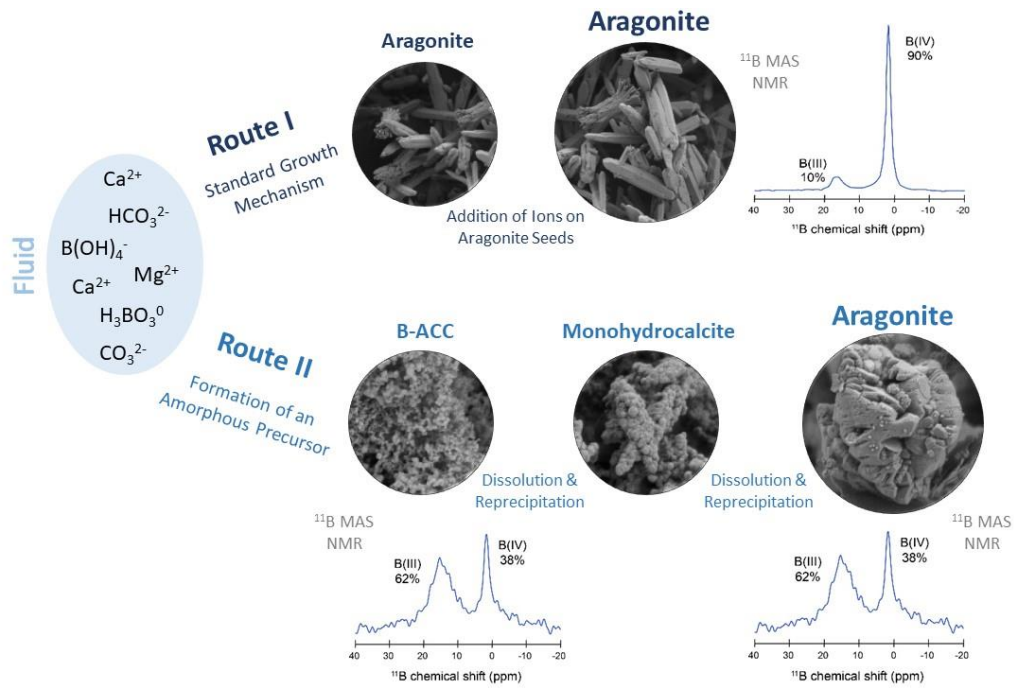


Figure 9: Illustration of the impact of aragonite crystallization route on B isotope fractionation between aragonite and aqueous borate. The data for the standard growth mechanism (route I) and the growth via the formation of a transient amorphous precursor are from Noireaux et al. (2015) and this study, respectively.